# CFD Simulation of Riser VIV

**by**

**Hamn-Ching Chen, Ocean Engineering Program, Department of Civil Engineering, Texas A&M University**

**Chia-Rong Chen, Department of Mathematics, Texas A&M University**

**Richard S. Mercier, Ocean Engineering Program, Department of Civil Engineering, Texas A&M University**

## Final Project Report

**Prepared for the Minerals Management Service**
**Under the MMS/OTRC Cooperative Research Agreement**
**1435-01-99-CA-31003**
**Task Order 74521**
**1435-01-04-CA-35515**
**Task Order 35983**
**MMS Project Number 481**

**December 2006**

OTRC Library Number: 10/2006A176




*For more information contact:*

**Offshore Technology Research Center**
Texas A&M University
1200 Mariner Drive
College Station, Texas 77845-3400
(979) 845-6000

or

**Offshore Technology Research Center**
The University of Texas at Austin
1 University Station C3700
Austin, Texas 78712-0318
(512) 471-6989

*A National Science Foundation Graduated Engineering Research Center*

# Table of Contents

# List of Tables and Figures

## Table



## Figures

# 1. Project Description

## 1.1 Background

Offshore oil/gas drilling and production operations face hazards due to the exposure of submerged rig components to underwater sea currents. Critical among these components are the marine risers, consisting of a series of long steel pipes of circular cross-section, used for deep-water extraction of oil and/or natural gas. These long cylindrical structures, exposed to strong sea currents, induce the flow around them to separate and initiate vortex shedding – whereby vortices of opposite sign are shed synchronously from the aft of the structure. The resultant lift and drag forces excite forced oscillations of the riser, known as vortex-induced vibrations (VIV). When the VIV frequency is close to one of the natural frequencies of the structure, a resonance phenomenon popularly known as "lock-in" occurs, resulting in enhancement of the vibration amplitude of the structure – and thus its destructive potential.

Since the VIV phenomenon is quite complex to model, the analysis of fluid-induced motions in deepwater has remained a somewhat empirical science. Currently, the design criteria and tools for the operation of marine risers under lock-in conditions rely on simplified mathematical models and/or anecdotal evidence. Increasing development costs and increasingly hostile field environments demand more robust, reliable, and refined design strategies and tools. This need has renewed interest in the study of the VIV phenomenon by experimentalists and numerical analysts.

Accurate fatigue life prediction requires knowledge of the frequency and magnitude of the vibration, in addition to average forces acting on the moving structure. Improved design principles for risers require an approach that can supplement existing empirical knowledge and experimental data. A promising approach is to use computational fluid dynamics to provide studies on fluid-induced motions of structures.

In operating conditions, the marine risers are subjected to flow conditions that correspond to high Reynolds number flows, typically $O(10^5) - O(10^7)$, and low structural mass ratio and damping. These conditions are difficult and expensive to achieve in an experimental setup, and thus an attractive alternative is to use computational fluid dynamics (CFD) tools to study/predict the response of the riser undergoing VIV. Unfortunately, well-established numerical procedures for CFD (e.g., finite elements, finite differences, and control volumes) are not robust with respect to high Reynolds number flows. As the Reynolds number increases, these methods are prone to developing spurious node-to-node oscillations – which eventually cause the numerical solution procedure to break down. The oscillations can be suppressed by refining the mesh, but the necessary degree of refinement is often prohibitively expensive. In view of this drawback, most of the previous work on simulations of the VIV phenomena have been limited to low Reynolds number flows, $O(10^2) - O(10^3)$.

## 1.2 Present Work

The objective of this research is to develop advanced CFD capabilities for improving the prediction of riser VIV responses at high Reynolds number. The performance of VIV suppression devices such as helical strakes and fairings is also evaluated. This report documents the following tasks accomplished under this project:

- Development of advanced CFD capabilities: numerical method and parallelization
- 2-D simulations of flow past a fixed riser at high Reynolds numbers
- Surface roughness effects
- 2-D simulations of elastically mounted risers undergoing VIV at high Reynolds number: single isolated riser and arrangements of multiple risers
- 3-D Large Eddy Simulation of flow past a fixed riser
- 3-D Large Eddy Simulation of an elastically mounted riser undergoing VIV
- Simulations of an elastically mounted riser outfitted with a fairing
- Simulations of an elastically mounted riser with helical strakes

The main thrust of this work is use of a novel and robust discretization procedure whereby the Navier-Stokes equations are discretized using local analytic solutions of the linearized problem (Pontaza, Chen and Reddy, 2005; Chen, Patel and Ju, 1991). The formulation is robust with respect to high Reynolds number flows, strong mesh skews, and is asymptotically second-order accurate. In addition, the formulation is implemented alongside the ability to treat embedded and non-matching grids, allowing for relative grid motion. This capability makes fluid-structure interaction problems easy to handle, as tedious grid re-generation is avoided by virtue of the ability to treat embedded meshes moving in fixed background grid components. Thus, the formulation is suitable to simulate the VIV phenomena – inherently a fluid-structure interaction problem at high Reynolds numbers.

In practical applications, the Reynolds number is large (typically $O(10^5) - O(10^7)$) and flow conditions are transitional or turbulent. Thus, the flow exhibits complex three-dimensional features, making analysis difficult and computationally expensive for direct numerical simulations of the governing incompressible Navier-Stokes equations. A more practical first-stage approach is to assume that the flow can be treated as two-dimensional and perform high resolution simulations at this level. These simulations are of great practical importance as they shed light on first-principles of fluid-induced motions and may improve design principles for deepwater risers. Two-dimensional simulations are presented in the first part of this work. In later stages of this work we will discard the two-dimensionality assumption, and perform fully three-dimensional simulations of short aspect ratio risers (L/D = 3 and 9). In real world applications, deepwater risers can easily exceed aspect ratios of L/D = 1000. For example, Holmes, Constantinides and Oakley (2006) presented fully-3D simulation results for a bare riser with L/D = 1400 and a straked riser with L/D = 1151. The computer resources currently available at Texas A&M University do not permit adequate resolution of fully 3D VIV of such L/D ratios since each user is allowed to use no more than 16 processors at a time. However, it

should be remarked here that the present method is currently being generalized in a new research project (2006-2008) for the simulation of flexible long risers.

In a recent study, we have successfully performed fully 3D simulations of a flexible riser with L/D = 1400 using very large grid spacing (L/D ~ 50) in the spanwise direction. These preliminary 3D simulations clearly demonstrated the feasibility of using the present CFD code in conjunction with a finite element tensioned beam model for simulation of flexible long risers even though the fluid interactions in the spanwise direction were not properly resolved with such a large spanwise spacing. With the availability of additional computer resources in the future, it is anticipated that the parallel computer program developed under this project can be readily employed for truly 3D simulations on large computer clusters with hundreds of dedicated processors.

## 2. Development of Advanced CFD Capabilities

From the computational viewpoint, simulations of riser VIV are fluid-structure interaction problems posed at high Reynolds numbers. Standard discretization methods such as finite volumes or Galerkin finite elements are not robust with respect to high Reynolds numbers, and tend to develop node-to-node spurious oscillations when the cell Reynolds number exceeds a certain threshold. Stabilization techniques (upwinding or subgrid stabilization) may be invoked to render the schemes stable, and are popular in practice. In addition, these methods typically need grid re-generation and/or control of element distortions as the structure moves on the fluid mesh. A more detailed review of various numerical methods is given in Pontaza, Chen and Reddy (2005).

In the present work, the governing incompressible Navier-Stokes equations are discretized using the local-analytic-based discretization procedure of Pontaza, Chen, and Reddy (2005), whereby local analytic solutions of the linearized advection-diffusion part of the momentum equations are obtained at the local (element) level and used to construct finite-difference-like stencils in terms of neighboring nodal degrees of freedom. The local analytic nature gives the resulting stencils suitable upwinding according to the local velocity field and element aspect ratio. In essence, the amount of upwinding is determined by virtue of the local analytic solution and not in a heuristic manner along gridlines. The two-dimensional 9-point stencil and the three-dimensional 19-point stencil allow for skew upwinding, depending on local flow conditions.

The incompressibility constraint is enforced by a discrete projection method which ensures proper velocity-pressure coupling. Time stepping is performed using a second-order stiffly stable backward differentiation scheme; popularly known as a BDF2 scheme. For low to moderate cell Reynolds numbers, the scheme is second order accurate in velocities and pressure. At arbitrarily high cell Reynolds numbers the scheme is always asymptotically second order accurate and unconditionally stable. Details of the discretization procedure, including verification and validation are presented in Pontaza, Chen, and Reddy (2005).

The numerical method is implemented in an overset (Chimera) grid environment. This allows for great flexibility in representing complex geometries and allows for surgical mesh refinements, in the form of overlapping and embedded groups of grid components. Individual structured grids are allowed to overlap arbitrarily, and inter-grid communication is achieved by mass conservative Lagrange interpolation at the fringes.

Figure 1 shows an instantaneous snapshot of a close-up view of the Chimera grid used for a multiple-riser VIV simulation. The different block-structured components are shown in different colors. The individual grid components around each riser can be refined independently from neighboring grid components, resulting in improved local resolution and overall computational savings (as the other grid components remain un-refined). The grids shown in Figure 1 are embedded in still coarser background grids (not shown in Figure 1) to represent the far-field.

The use of any kind of wall functions is avoided and the boundary layer is resolved by using fine grid spacing around the riser surface in conjunction with the no-slip boundary condition. The first grid point in the normal direction of the grid wrapped around the risers is typically placed at a distance of 10/Re from the body. In terms of wall coordinates, we place the first grid point at a distance of $y^+ = U_\tau \, y / \nu \leq 0.50$ for the range of Reynolds numbers considered, where $U_\tau$ is the friction velocity, $y$ is the normal distance from the wall and $\nu$ is the kinematic viscosity of the fluid. A minimum of 15 grid points are used to cover the viscous sub-layer and provide adequate resolution of the boundary layer and near wake flows around the riser.

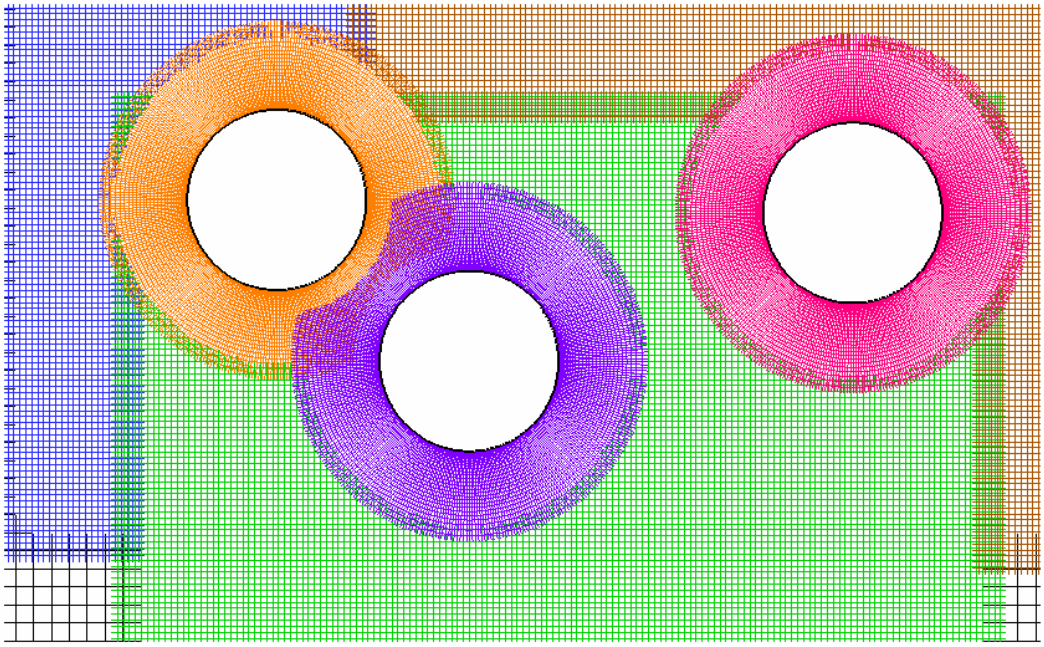

**Figure 1. Instantaneous snapshot of overset grid for simulation of multiple-riser VIV**.

The turnaround time of the simulations is accelerated by further exploiting the multiple-block data structure of the code and the Chimera approach. Using MPI (Message-Passing-Interface) bindings, we are able to distribute the workload associated with different blocks among different processors working in parallel. Specifically, different numbers of blocks can be assigned to different processors. Load balancing is the task of the user, but the structure of the code facilitates this task by allowing single or arbitrarily large groups of consecutive or non-consecutive blocks to be assigned to different processors. The simulations performed in this work were executed using 4 to 16 processors working in parallel. As noted earlier, it was not possible to use additional processors at the present time due to the university resource restrictions and established quotas.

When the risers undergo two or three degree-of-freedom VIV, the meshes shown in Figure 1 move on top of earth-fixed background Cartesian meshes, thus avoiding tedious grid-regeneration and/or mesh distortion monitoring. The interpolation stencils that are needed to communicate across grid components are simply updated as the grid moves.

For the range of Reynolds numbers considered in our studies, a detailed resolution of all turbulence length and time scales using the Direct Numerical Simulation (DNS) approach would be prohibitively expensive and our grids may be deemed inappropriate as they would not satisfy the strict resolution requirements. For the flow simulations around $Re=10^5$ we use a Large Eddy Simulation (LES) approach with the Smagorinsky eddy-viscosity model to account for the unresolved small turbulent scales. At these sub-critical Reynolds numbers the boundary layer is still transitional, and LES provides appropriate resolution of the large scale turbulent eddies in the riser wake.

For flows around and greater than $Re=10^6$, we assume a fully turbulent boundary layer and use the Reynolds-Averaged Navier-Stokes (RANS) equations with the two-layer k-ε model of Chen and Patel (1988) to account for turbulence effects. In general, RANS simulations provide accurate resolution of the turbulent boundary layer and near wake for high Reynolds flows with thin shear layers, but tends to smooth out the chaotic motion of the large eddies in the far wake due to the ensemble average (i.e., Reynolds average) of the highly unsteady instantaneous velocity and pressure fields. It is worthwhile to note that the riser response to VIV is determined primarily from the drag, lift, and moments exerted on the risers by the oncoming fluid, therefore it is anticipated that the chaotic motion of the far wake will not significantly change the drag and lift or alter the riser VIV motion. Since we are mostly interested in the accurate prediction of the riser VIV response, it is justified to use unsteady RANS equations which provide appropriate resolution of the lift and drag forces exerted on the risers for high Reynolds number flow conditions.

The governing equations for a Large Eddy Simulation (LES), in non-dimensional form, are

$$\frac{\partial u_i}{\partial x_i} = 0$$

$$\frac{\partial u_i}{\partial t} + u_j \frac{\partial u_i}{\partial x_j} + \frac{\partial p}{\partial x_i} - \frac{\partial}{\partial x_i}\left\{\left(\frac{1}{\mathrm{Re}} + \nu_t\right)\left[\frac{\partial u_i}{\partial x_j} + \frac{\partial u_j}{\partial x_i}\right]\right\} = 0$$

where the turbulent viscosity is defined as $\nu_t = \ell^2 |S|$, where $|S|$ is the magnitude of the strain-rate tensor. Here $\ell$ is the subfilter length scale, given by $\ell = C_s \Delta$, where $C_s$ is the Smagorinsky constant and $\Delta$ is the filter width. Here we use the standard value for the Smagorinsky constant, $C_s = 0.10$. In three-dimensional simulations the filter length is typically taken as the cubic root of the cell volume enclosing the grid point under

consideration. For two-dimensional simulations, we simply take the square root of the cell area as a representative filter length.

The unsteady Reynolds-Averaged Navier-Stokes (RANS) equations used in conjunction with the standard k-ε turbulence model are written as follows

$$\frac{\partial u_i}{\partial x_i} = 0$$

$$\frac{\partial u_i}{\partial t} + u_j \frac{\partial u_i}{\partial x_j} + \frac{\partial p}{\partial x_i} - \frac{1}{\mathrm{Re}} \frac{\partial^2 u_i}{\partial x_j \partial x_j} - \frac{\partial \tau_{ij}}{\partial x_i} = 0$$

$$\frac{\partial k}{\partial t} + u_i \frac{\partial k}{\partial x_i} - \frac{\partial}{\partial x_i}\left\{\left(\frac{1}{\mathrm{Re}} + \nu_t\right)\frac{\partial k}{\partial x_i}\right\} - G - \varepsilon = 0$$

$$\frac{\partial \varepsilon}{\partial t} + u_i \frac{\partial \varepsilon}{\partial x_i} - \frac{\partial}{\partial x_i}\left\{\left(\frac{1}{\mathrm{Re}} + \frac{\nu_t}{\sigma_\varepsilon}\right)\frac{\partial \varepsilon}{\partial x_i}\right\} - C_{\varepsilon 1} G \frac{\varepsilon}{k} - C_{\varepsilon 2} G \frac{\varepsilon^2}{k} = 0$$

with the following definitions for the Reynolds stress tensor $\tau_{ij}$, rate of strain tensor $S_{ij}$, production term $G$, and eddy viscosity $\nu_t$:

$$\tau_{ij} = -\frac{2}{3} k \delta_{ij} + 2 \nu_t S_{ij}$$

$$S_{ij} = \frac{1}{2}\left(\frac{\partial u_i}{\partial x_j} + \frac{\partial u_j}{\partial x_i}\right)$$

$$G = 2 \nu_t S_{ij} S_{ji}$$

$$\nu_t = C_\mu \frac{k^2}{\varepsilon}$$

and the standard model constants are used ($C_{\varepsilon 1}, C_{\varepsilon 2}, \sigma_\varepsilon, C_\mu$) = (1.44, 1.92, 1.3, 0.09). We use the two-layer k-ε turbulence model of Chen and Patel (1988), where a k-ℓ model is used in the near wall region and patched with the standard k-ε model in the buffer layer. In the near wall region, the k-ℓ model uses a wall damping function parameterized in terms of the turbulent kinetic energy which makes it robust for flows with massive separation, such as the flows considered in this study.

## 3. Two-Dimensional Simulations of Flow Past a Fixed Riser

We consider the two-dimensional flow of an incompressible fluid past a smooth rigid riser. At low Reynolds numbers ($5 < Re < 40$) the flow is stationary and characterized by a pair of standing vortices appearing behind the riser. The size of the separated flow region increases with increasing Reynolds number, until a limit in which the wake becomes unstable. At this critical Reynolds number, $Re_c \sim 46.2$, vortices are shed from the aft of the riser, forming the well-known von Karman vortex street.

We wish to test the predictive capabilities of the formulation for a wide range of Reynolds numbers, and especially at high Reynolds numbers. To this end a set of simulations was executed spanning the Reynolds number range $O(10^1) - O(10^7)$, which covers sub-, trans-, super-, and post-critical flow regimes for separated flows around bluff bodies. In spite of the fact that the flow is no longer two-dimensional above $Re \sim 188.5$, we expect the simulation results to qualitatively follow experimentally observed behavior for the time-averaged drag coefficient.

The computational domain is configured sufficiently large to preclude unwanted effects on computed flow metrics due to blockage, or location of inflow and outflow boundaries. The computational domain extends from -15D at the inlet to 20D at the outlet and from -15D to 15D in the crossflow direction, where D is the riser diameter.

Boundary conditions include free-stream values assigned at the inflow boundary, a no-flux or symmetry boundary condition at the lateral boundaries, no-slip boundary conditions on the riser-fairing surface, and non-reflective outflow boundary conditions. Boundary conditions on the pressure are not explicitly necessary, and are recovered as part of the velocity projection step (Pontaza, Chen and Reddy, 2005). In other words, pressure is consistently computed at all boundaries.

Figure 2 shows the computed drag vs. Reynolds number data, alongside data from experimental measurements. We plot results obtained in successively finer meshes: M1 (coarse) through M4 (fine). Very good qualitative agreement with the experimental measurements is observed throughout the entire Reynolds number range considered, and we are able to predict the drag crisis that occurs during critical transition and the super-critical flow regime. The two-dimensional simulations are not able to predict the drag recovery in the post-critical regime, and we conjecture that a three-dimensional simulation would be better suited for this regime.

Plots of the one-dimensional energy spectra of velocity recorded 0.25 riser diameters from the base of the riser (i.e., $\theta = 180°$) are shown in Figure 3 for $Re = 10^5$ and $Re = 10^6$ flows using M3 resolution. Streamwise and cross-flow velocities were recorded over a time interval of 50 convective time units and their energy spectra is shown in Figure 3. The frequency is normalized by the dominant shedding frequency, or Strouhal frequency at the corresponding Reynolds number. At $Re = 10^5$ the energy spectrum shows the expected slope of $-3$ (for "two-dimensional turbulence") in the

inertial subrange, indicating that M3 resolution is adequate at this Reynolds number. The grid is able to resolve scales with frequencies up to an order of magnitude higher than the dominant frequency. Thus, M3 resolution will be used for the VIV simulations in this study, which are limited to $Re \leq 10^5$.

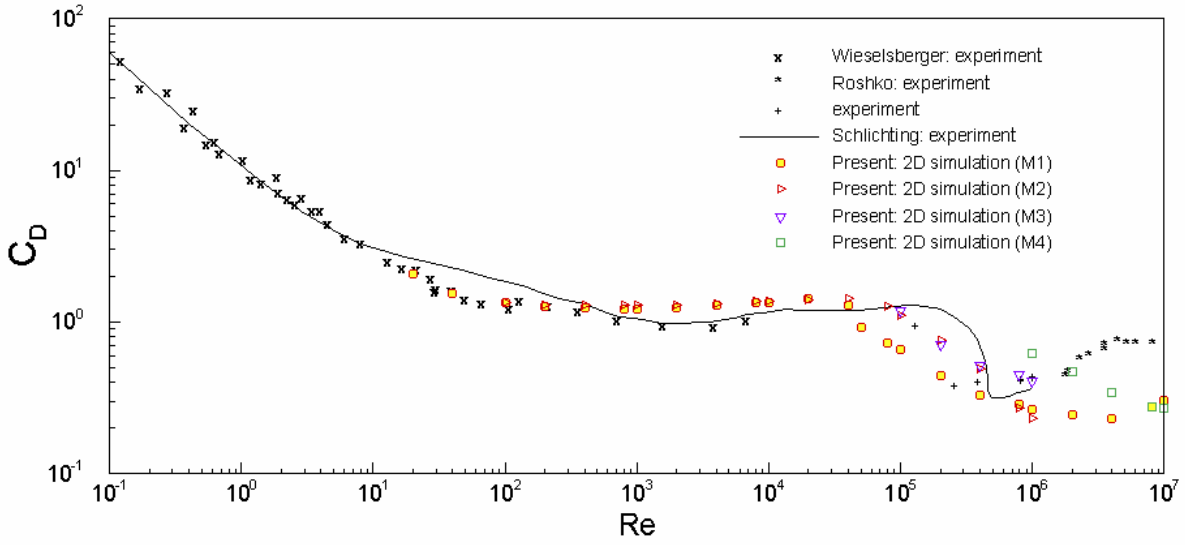


**Figure 2. Time-averaged drag coefficient vs. Reynolds number curve.**

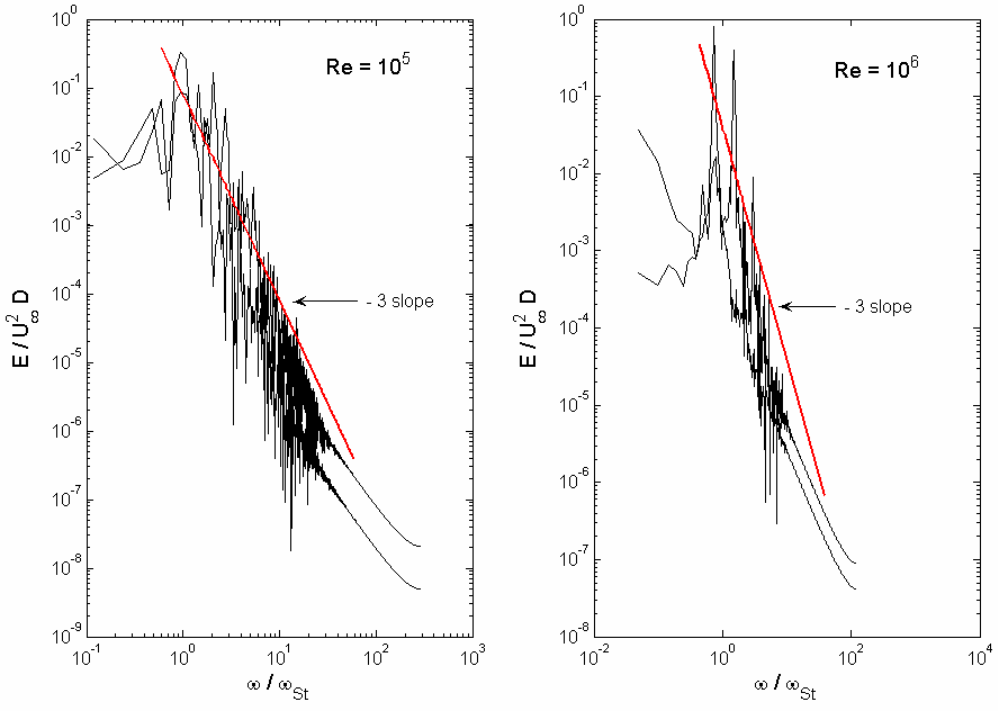


**Figure 3. Energy spectra of velocity fluctuations using M3 resolution at two high Reynolds numbers. M3 resolution is not adequate at $Re = 10^6$.**

In contrast, at Re = $10^6$ the energy spectra departs significantly from the –3 slope. The medium to small scales are not represented correctly due to lack of spatial resolution at this Reynolds number. A plot of the one-dimensional energy spectra of velocity fluctuations at the same location as before is shown in Figure 4 for Re = $10^6$, now using M4 resolution. The energy spectrum shows the –3 slope in the inertial subrange, indicating that M4 resolution is adequate at this Reynolds number.

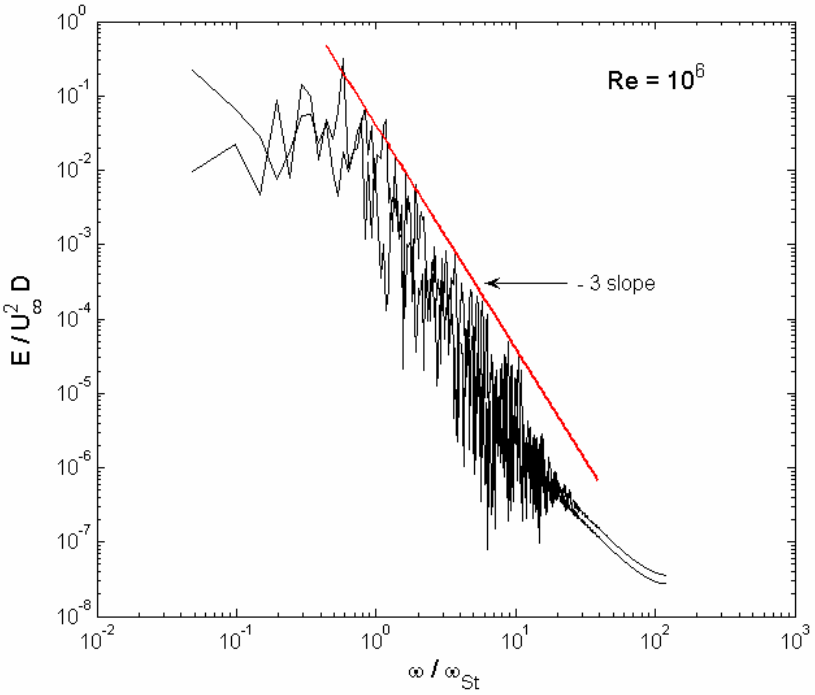


**Figure 4. Energy spectra of velocity fluctuations using M4 resolution at Re = $10^6$.**

We note that the near-wall grid spacing used around the risers was such that the Smagorinsky eddy viscosity in these areas was negligibly small (i.e. $\nu_t$ was less than 1/Re when checked in the post-processing stage). This simply means that the grid spacing in the near-wall was small enough to adequately resolve medium to small eddy scales. Simulations without the LES sub-grid scale model (i.e., equivalent to DNS) gave nearly identical results for the drag and lift coefficients.

# 4. Surface Roughness Effects

A considerable amount of time was allocated to review and implement roughness models available in the open literature. Here, we document results using the two-layer k-ε turbulence model of Durbin et al. (2001) with surface roughness modifications and the two-layer k-Ω model of Patel and Yoon (1995) with surface roughness boundary conditions.

The two-layer k-ε turbulence model makes use of the standard k-ε turbulence model away from the solid surface and switches to a one-equation k-ℓ model in the near-wall region, where the length scale is determined analytically through van-Driest type damping functions that enforce the asymptotically correct behavior as the wall is approached. The van-Driest type functions are parameterized in terms of a velocity scale based on the turbulent kinetic energy, which is well defined during separation, rendering the model suitable for simulations where significant separation occurs. Unfortunately, the surface roughness modifications for the two-layer k-ε turbulence model are parameterized in terms of the wall-shear stress, which is ill-defined during separation.

The two-layer k-Ω turbulence model makes use of the standard k-ε turbulence model away from the solid surface and switches to a k-Ω model in the near-wall region. Thus, in the near-wall region a two-equation approach is retained. Modifications to model surface roughness are not needed, since the effects are readily accounted for by simply making use of "rough-wall" boundary conditions for the field variable Ω. Unfortunately, the surface roughness boundary condition is directly correlated with the wall-shear stress, which is ill-defined for separated flows.

The flow past a riser is a flow with massive separation, and thus it was found after extensive experimentation that roughness models parameterized in terms of the wall-shear stress may not be accurate in these cases. Figure 5 shows the time history of the drag coefficient at $\mathrm{Re} = 10^6$, for a smooth and rough riser, computed using the two-layer k-ε model. Similarly, Figure 6 shows results obtained using the two-layer k-Ω model.

In accordance with experimental data, at this Reynolds number the effect of surface roughness is to increase the drag coefficient. However, the observed increase in drag is less pronounced than that observed in experiments for the same flow conditions and roughness ($k_s/D = 0.0025$). In addition, the results obtained with the two turbulence models differ slightly from each other for both smooth and rough cases.

Thus, there is a need for the development of a new roughness model, parameterized in terms of the turbulent kinetic energy, which remains well-defined even for massively separated flows. We would expect to obtain much better predictions with such a roughness model.

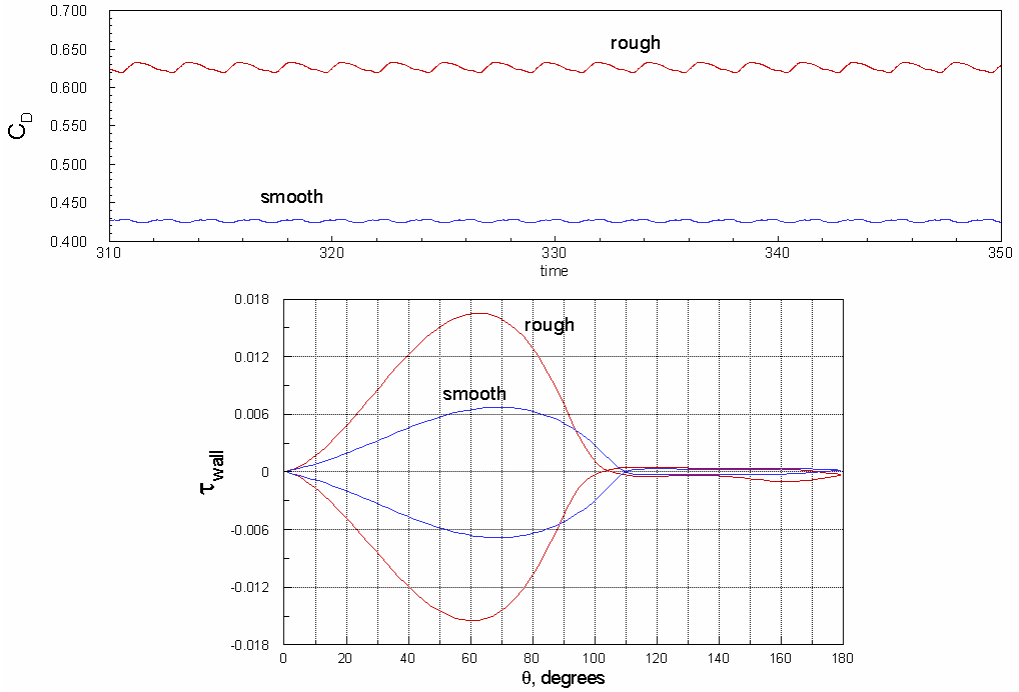


**Figure 5. Two-layer k-ε roughness model results.**

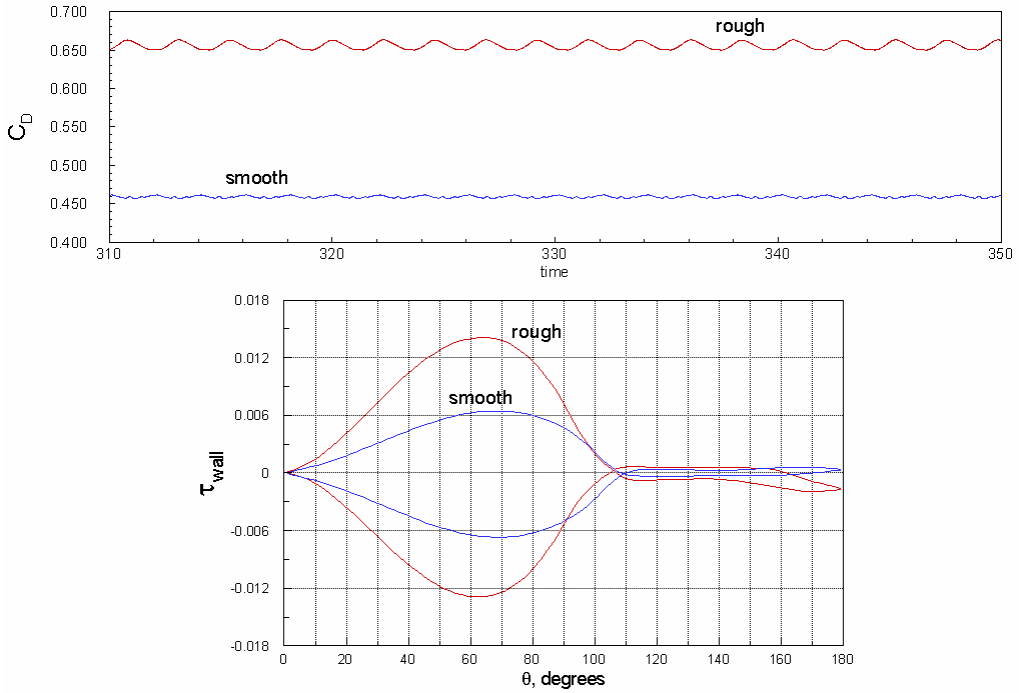


**Figure 6. Two-layer k-Ω roughness model results.**

## 5. Two-Dimensional Simulations of Elastically Mounted Risers Undergoing VIV

The riser is now left free to respond to the flow field. The structural response of the risers is assumed to be governed by a mass-spring-damper system in the $X$ and $Y$ directions as follows:

$$m\ddot{X} + c\dot{X} + kX = f_X$$

$$m\ddot{Y} + c\dot{Y} + kY = f_Y$$

where $m$ is the mass of the riser, $c$ is the structural damping coefficient, $k$ is the spring constant, and ($f_X$, $f_Y$) are the ($X$, $Y$) component forces exerted on the riser by the ambient fluid. The above equations are normalized by the fluid density $\rho$, ocean current velocity $V$, riser diameter $D$ and riser length $L$ using the following set of dimensionless variables:

$$x = \frac{X}{D} \; ; \quad y = \frac{y}{D} \; ; \quad t = \frac{V\,T}{D}$$

$$m^* = \frac{m}{m_d} \; ; \quad m_d = \rho \frac{\pi}{4} D^2 L$$

$$\zeta^* = \frac{c}{c_{critical}} = \frac{c}{2\sqrt{k\,m}}$$

$$U^* = \frac{V\,D}{f_n} \; ; \quad f_n = \frac{1}{2\pi}\sqrt{\frac{k}{m}}$$

$$C_D = \frac{f_x}{\frac{1}{2}\rho V^2 D\,L} \; ; \quad C_L = \frac{f_y}{\frac{1}{2}\rho V^2 D\,L}$$

where $x$ and $y$ are the dimensionless displacements and $t$ is the dimensionless time. $m^*$ is the mass ratio normalized by the displaced fluid mass $m_d$. $\zeta^*$ is the structural damping ratio, $U^*$ is the reduced velocity, $f_n$ is the natural frequency of the vibrating riser, and $C_D$ and $C_L$ are the instantaneous drag and lift force coefficients acting on the riser. The dimensionless equations of motion for the riser under two degree-of-freedom VIV motion can be written as

$$\ddot{x} + \frac{4\pi\zeta^*}{U^*}\dot{x} + \left(\frac{2\pi}{U^*}\right)^2 x = \frac{2}{\pi}\frac{C_D(t)}{m^*}$$

$$\ddot{y} + \frac{4\pi\zeta^*}{U^*}\dot{y} + \left(\frac{2\pi}{U^*}\right)^2 y = \frac{2}{\pi}\frac{C_L(t)}{m^*}$$

It is worthwhile to note that the problem of riser VIV is essentially a fluid-structure interaction problem, where the structure responds instantaneously to the fluid-induced lift and drag forces. These forces are computed using the instantaneous velocity and pressure fields at each time step, by performing a numerical integration around the circumference of the riser. The riser is then displaced at each time step, by numerically solving the structure's equations of motion, and the flow-field time-advanced and re-computed to yield new instantaneous lift and drag forces.

The overset grid capabilities allow for relative motion between grid components, allowing for arbitrarily large motions of the riser without the need for tedious and costly grid re-generation and/or mesh deformation monitoring. In essence, the grid wrapped around and/or attached to the structure moves freely inside earth-fixed background meshes. Boundary interpolation stencils to communicate between grid components are re-computed every time step to ensure a continuous solution across grid fringes. In the present study, the structure's equations of motion are numerically integrated in time using a fourth-order accurate Runge-Kutta scheme.

We are interested in the structure's response for low mass and damping. The values for the mass ratio, damping ratio, and reduced velocity used for the simulations in this study are: $m^* = 1.0$, $\zeta^* = 0.005$ and $U^* = 6.055$, at flow conditions of Reynolds number $\mathrm{Re} = V D / \nu = 10^5$.

### 5.1 Single Riser

The riser is first held stationary until the shedding has reached full-strength – at which point the riser is "released" and allowed to respond to the flow field. Figure 7 shows the *X*-*Y* response of the riser for the first 100 convective time units, where time is implicit in the plot. Initially the riser is pushed downstream due to the acting drag force exerted by the oncoming fluid. Almost immediately, the riser responds to the acting lift forces and starts displaying strong cross-stream oscillations. Once the pattern of motion has settled, the *X*-*Y* response displays average peak-to-peak cross-stream amplitudes of 3.0 riser diameters. There is also strong in-line motion with average peak-to-peak amplitudes of 1.0 riser diameters. The response is remarkably stable and corresponds to a "figure-of-eight'" pattern which was maintained throughout the simulation time of 500 convective time units.

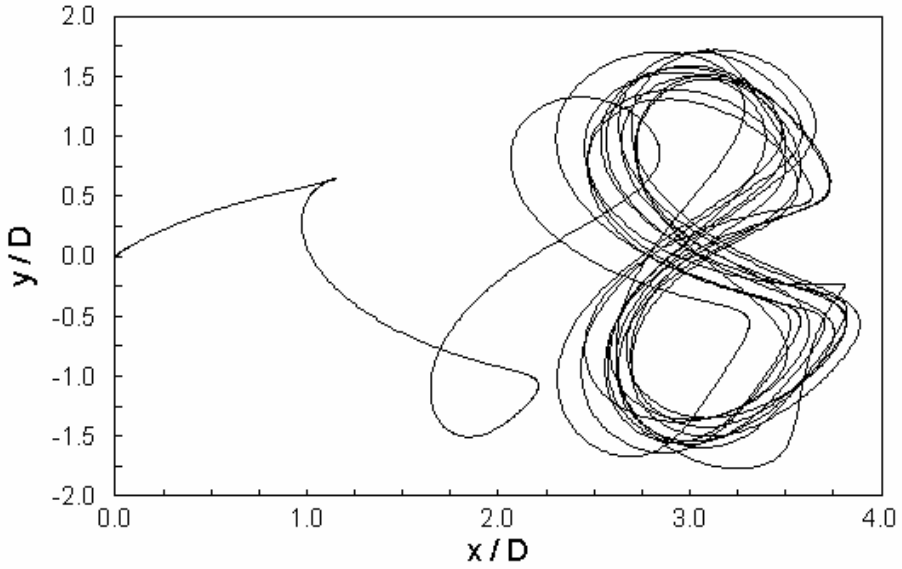


**Figure 7. X-Y response of elastically mounted riser undergoing VIV.**

The response displays characteristics of the recently discovered "super-upper" branch (see Jauvtis and Williamson, 2004) for light bodies ($m^* < 6.0$) undergoing two degree-of-freedom VIV. Although the experiments of Jauvtis and Williamson (2004) were conducted at lower Reynolds numbers (Re = $10^3$ – $10^4$), the predicted response clearly displays characteristics of the super-upper branch. In particular, the simulation result shows remarkably high cross-stream amplitudes and the 2T mode of vortex shedding to be described below.

Analysis of the power spectrum of the time history of body motion gives $f_X / f_Y = 2.0$, i.e. the streamwise oscillation frequency is twice that for the transverse (cross-stream) direction. In addition, although the body motion is not perfectly periodic, we find that a good representation of the average displacement pattern in the simulation is given by the following data fit,

$$y(t) = A_Y \sin(\omega t) \qquad x(t) = A_X \sin(2\omega t + \theta)$$

where $A_Y$ is the average cross-stream amplitude of vibration, $A_X$ is the average streamwise amplitude of vibration, $\omega = 2\pi f_Y$, and $\theta$ is the phase angle.

The following coefficients were extracted from the predicted time history response of our simulation: $A_Y = 1.540$, $A_X = 0.540$, $f_Y = 0.140$, and $\theta = -18°$. Figure 8 shows a plot of the fit, superimposed on the actual XY response. The fit is representative of the data, although not perfect. Note that instantaneous cross-stream and streamwise amplitudes reached values as high as $A_Y = 2.07$ and $A_X = 0.94$, respectively.

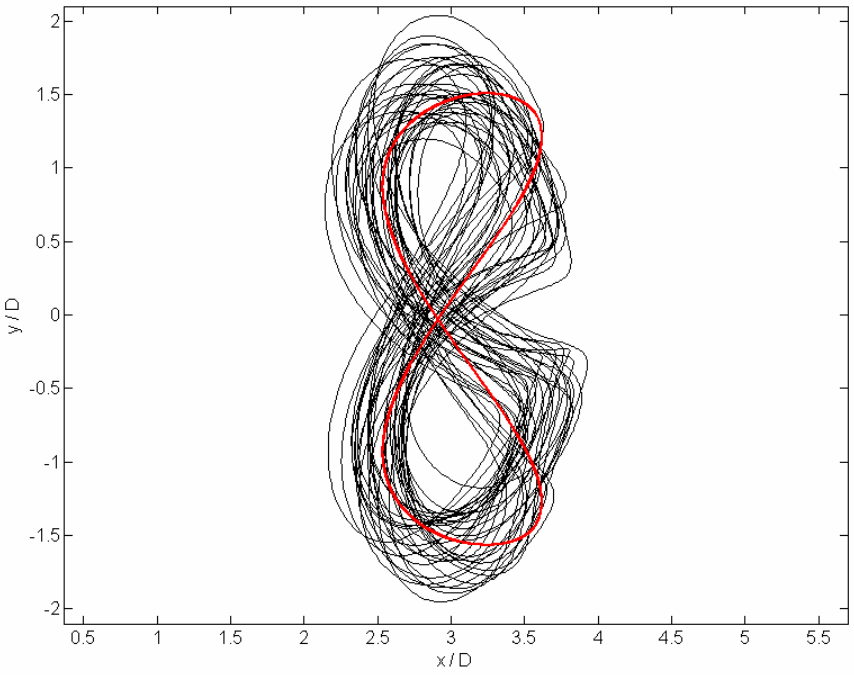


**Figure 8. Fit of VIV response (red), superimposed on the actual response (black).**

Our simulations indicate that the riser sheds 2 triplets of vortices per cycle of body motion. Figure 9 shows instantaneous vorticity contours during a cycle of body motion at time intervals of one dimensionless time unit. The "figure-of-eight" pattern for the cycle is overlaid on the figures to depict the vortex dynamics at each point during the cycle.

In Figure 9a we observe vortices 1 and 2, comprising a counter rotating vortex pair. In addition, we observe a third principal vortex (labeled as 3), which is generated in addition to the classical counter rotating vortex pair. The extra vortex 3 is a signature of the markedly different system response dynamics for bodies undergoing X-Y motions.

A second set of vortex triplets is shed when the body changes cross-stream direction, as shown in Figure 9d. From Figures 9c and 9d, we can see that the significant acceleration of the body at the top of the cycle generates vortices 2 and 3. This new mode of vortex shedding has been coined the 2T mode by Williamson and Jauvtis (2004), as two triplets are shed per cycle of body motion.

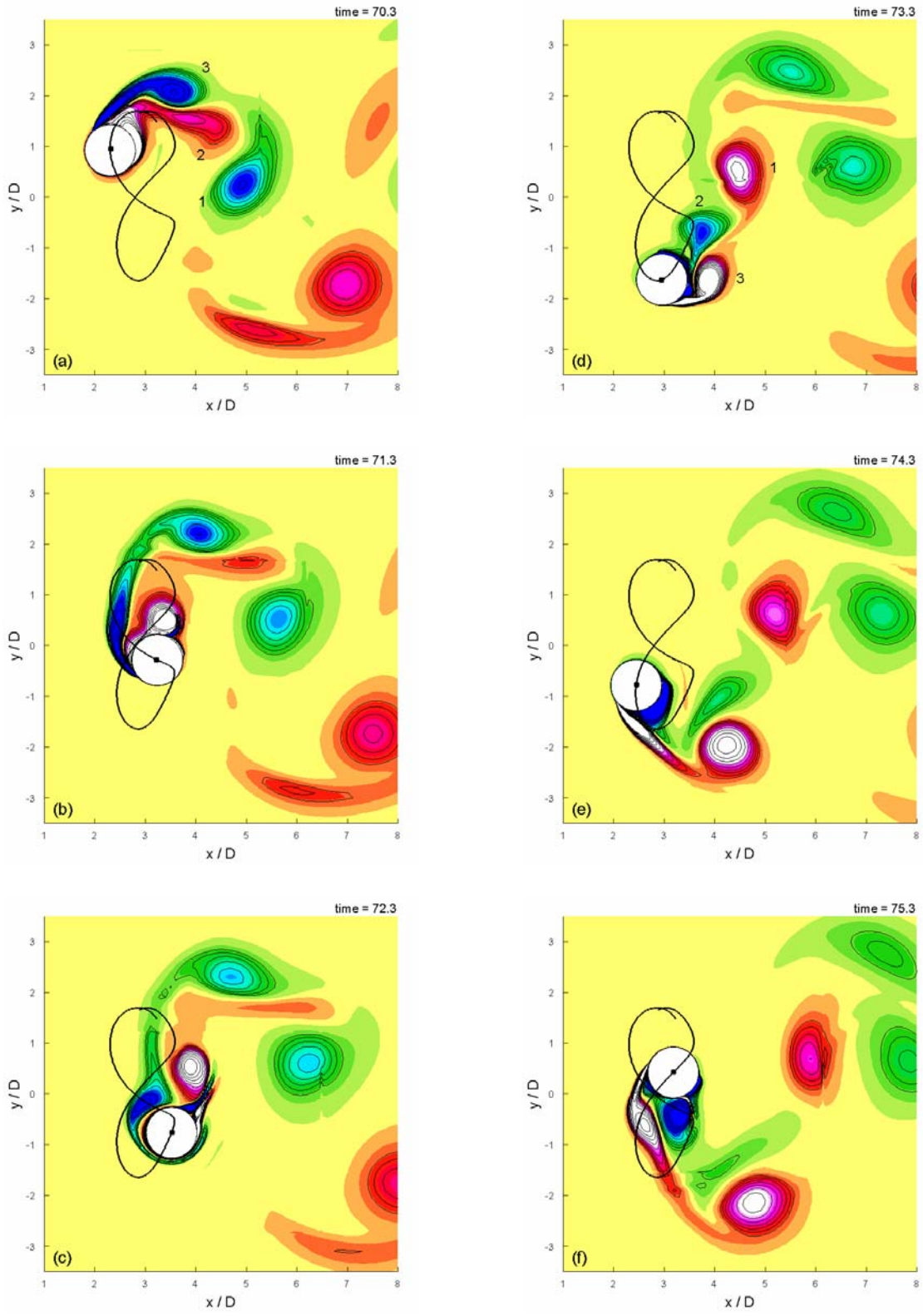


**Figure 9. Vorticity contours during a cycle of body motion for VIV of an isolated riser: (a)-(f). 2T vortex wake mode.**

In addition to the interesting body dynamics, a pronounced increase in the drag coefficient is observed. The time history of the drag and lift coefficients is shown in Figure 10 for 200 convective time units. The significant increase in drag is attributed to the strong in-line and transverse motions of the riser and is due to the fluid that must be displaced by the riser when moving against the oncoming free-stream. The average drag coefficient is 5.20 due to a significantly higher relative velocity between the riser and the ocean current. An energy spectrum analysis of the time history of the lift coefficient indicates two leading harmonics, $St_1 = 0.14$ and $St_2 = 3 \times St_1$.

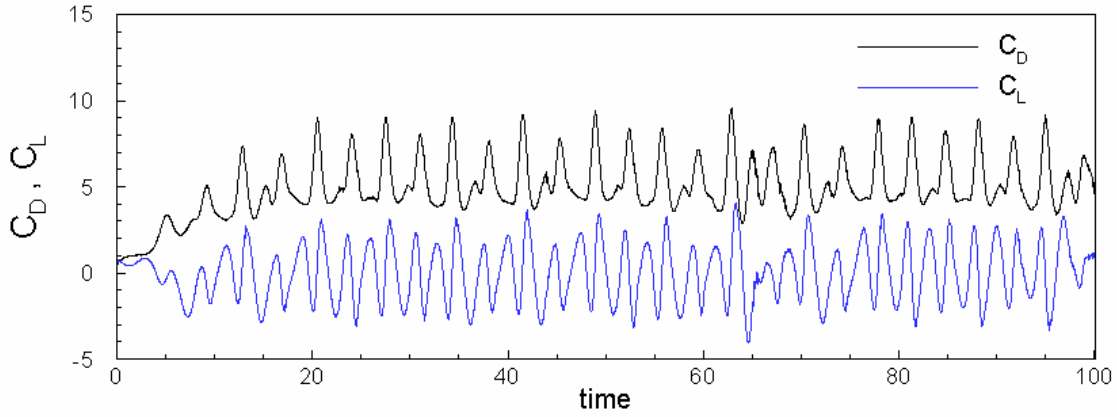


**Figure 10. Time history of drag and lift coefficients for an elastically mounted riser undergoing VIV.**

### 5.2 Risers in Tandem

With increasing water depth, the risers experience much larger in-line and lateral displacements under current force. This imposes a great challenge for the riser system design, especially when a large number of top tensioned risers are planned. In order to improve our understanding of the riser interference in deepwater applications, it is desirable to simulate the interactions of two risers in tandem and side-by-side arrangements.

For the tandem arrangement the initial center-to-center spacing considered is T/D=5.5. For fixed risers at this spacing, the flow falls in the wake interference regime (see Zdravkovich, 2003), where the upstream riser sheds vortices that impinge on the downstream one and the eddy streets are synchronized in frequency.

These simulations are computationally more demanding than those for an isolated riser, as the wake behind the upstream riser must be well resolved to allow for an accurate "inflow" to the downstream riser. For these runs we use higher resolution grids around the risers, with refined near-wake grids with uniform spacing of 0.015D.

The risers are left free to respond to the flow field once the shedding has reached full-strength for the fixed case. Figure 11 shows the predicted X-Y response of the risers for the first 100 convective time units, where time is implicit in the plot.

The upstream riser responds very much like an isolated riser with average peak-to-peak cross-stream amplitudes of 3.0 riser diameters. Like for the isolated case, the response is remarkably stable, despite the very high amplitudes of the body vibration. The body motion corresponds to a "figure-of-eight'" pattern which was maintained throughout the simulation time of 500 convective time units.

Although the response of the upstream riser is not perfectly periodic, the $x(t)$ and $y(t)$ data fit described earlier still provides a representative fit to the response. The following coefficients, for use in the fit, were extracted from the predicted time history response of the upstream riser: $A_Y = 1.460$, $A_X = 0.510$, $f_Y = 0.132$, and $\theta = -20°$. Thus, at the initial spacing T/D = 5.5, the downstream riser has negligible effects on the response of the upstream riser, which essentially responds like an isolated riser.

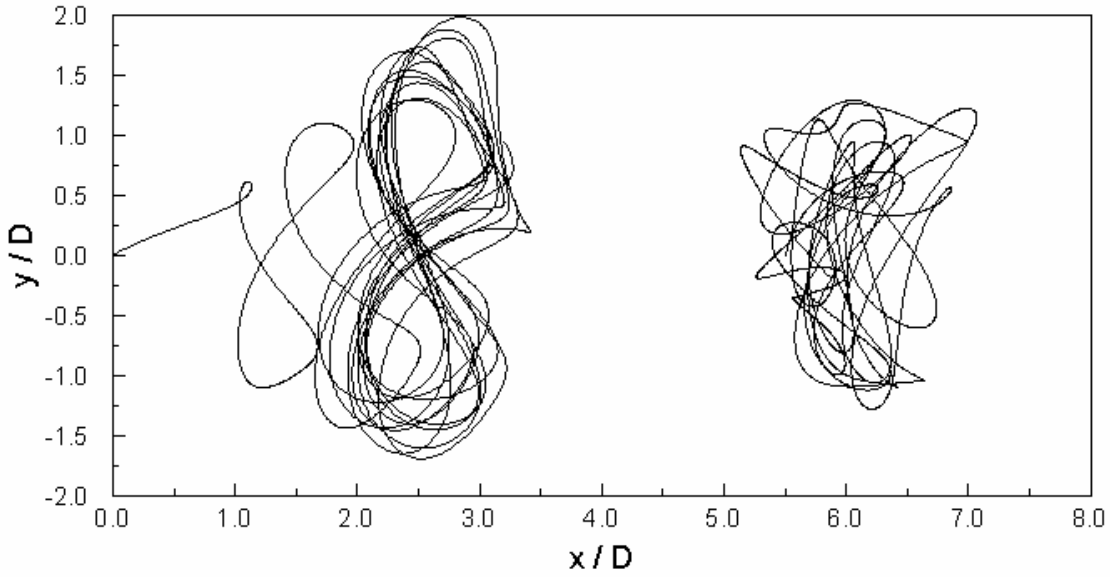


**Figure 11. X-Y response of VIV for risers in tandem with initial spacing T/D = 5.5.**

In contrast, the downstream riser displays a disorganized response and experiences wake-induced oscillations (as opposed to vortex-induced vibrations). Nevertheless, significant cross-stream and in-line oscillation amplitudes are observed. The disorganized response of the downstream riser was also reported by Mittal and Kumar (2000) for simulations at lower Reynolds number and higher mass ratio.

Figure 12 shows instantaneous vorticity contours during a cycle of body motion of the upstream riser. The vorticity is post-computed independently in each grid component from the velocity field (i.e. vorticity is not made continuous across grid components). Some noise is evident in transitions between grid components, and is due to the abrupt change in length-scale used to post-compute the vorticity.

The upstream riser sheds vortices in the 2T mode, which impinge on the downstream riser. The predicted time averaged drag coefficients are 4.43 for the upstream riser and 1.12 for the downstream one.

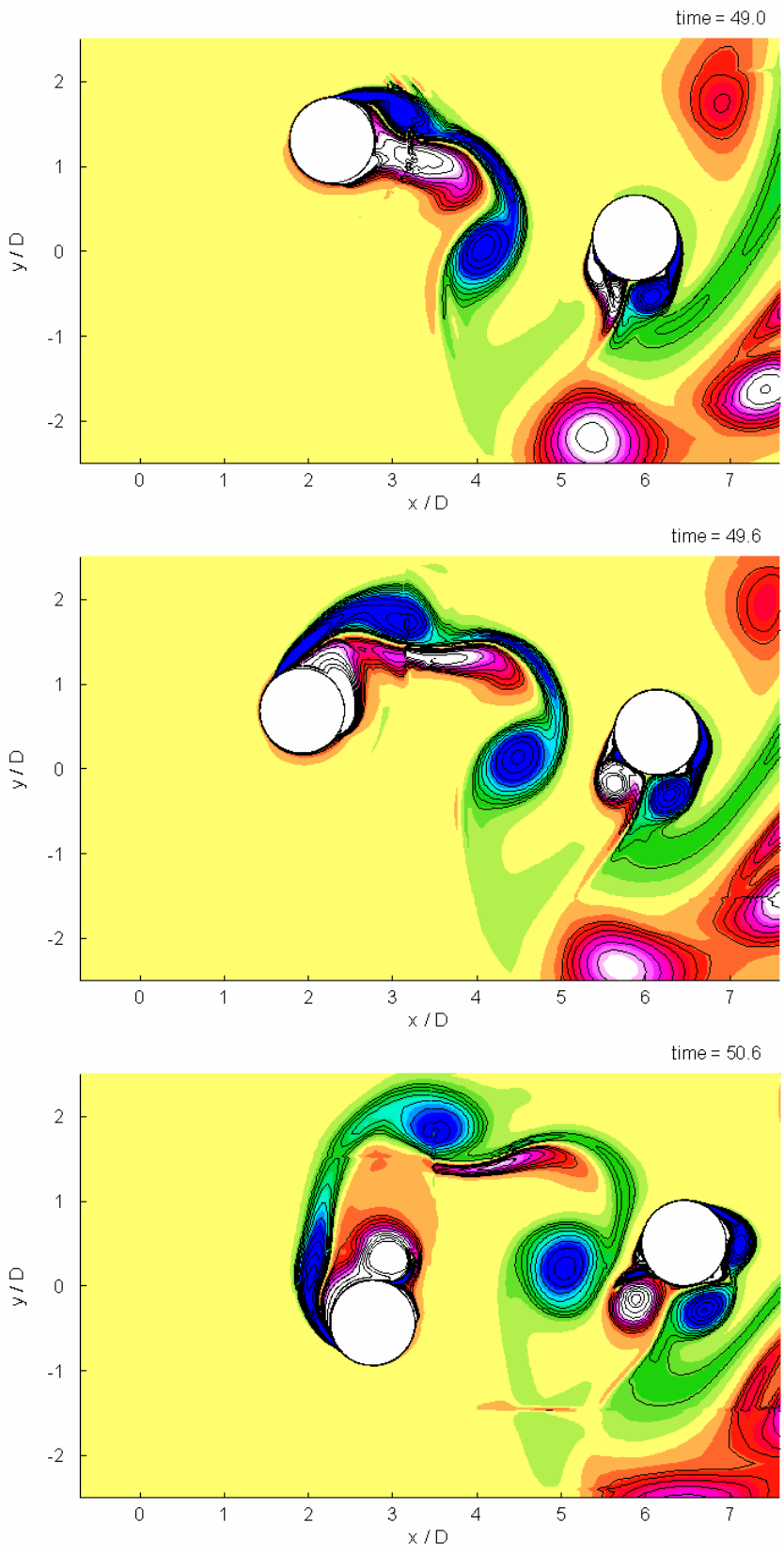


**Figure 12. Vorticity contours for VIV of risers in tandem.**

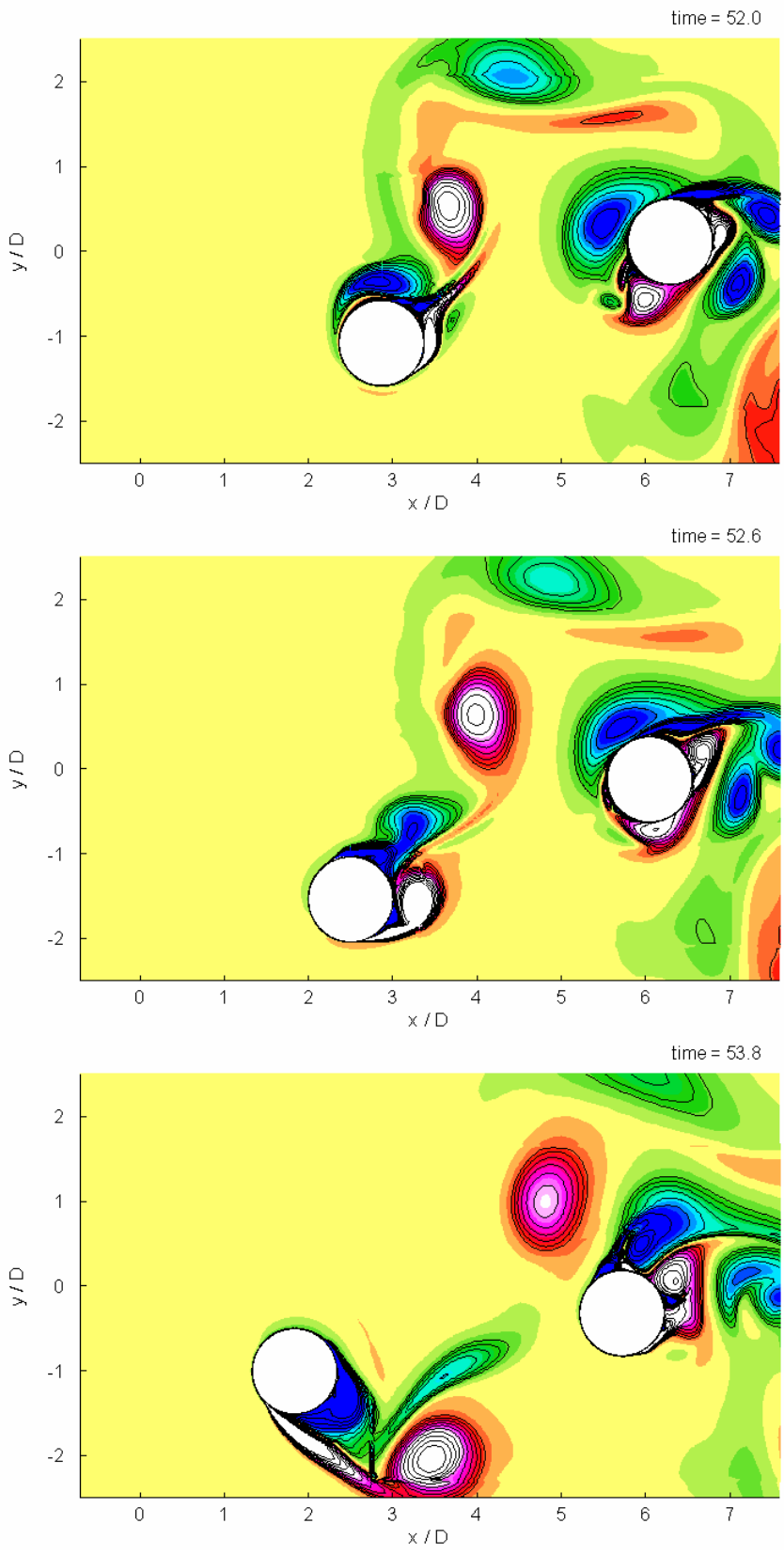


**Figure 12. (continued) Vorticity contours for VIV of risers in tandem.**

### 5.3 Risers in Side-by-Side Arrangement

For the side-by-side arrangement the initial center-to-center spacing is S/D=5.5. For fixed risers at this spacing, there is no interaction between the wakes of the two risers and the shedding can occur in two possible synchronized modes, either in-phase or anti-phase (Zdravkovich, 2003; Williamson, 1985).

Like for the tandem arrangement, the risers are left free once the shedding has reached full-strength for the fixed case. Interestingly, once the risers were left free, the shedding switched to in-phase and the risers responded to the flow field like isolated risers tracing "figures-of-eight" in-phase with each other. Thus, the risers never came close to each other for the simulation time considered because their motion was also in-phase.

Figure 13 depicts the in-phase motion observed in our simulation with an initial spacing of S/D=5.5. The "figure-of-eight"' patterns of the cycle of body motion are stable and no interaction between the risers was noticeable.

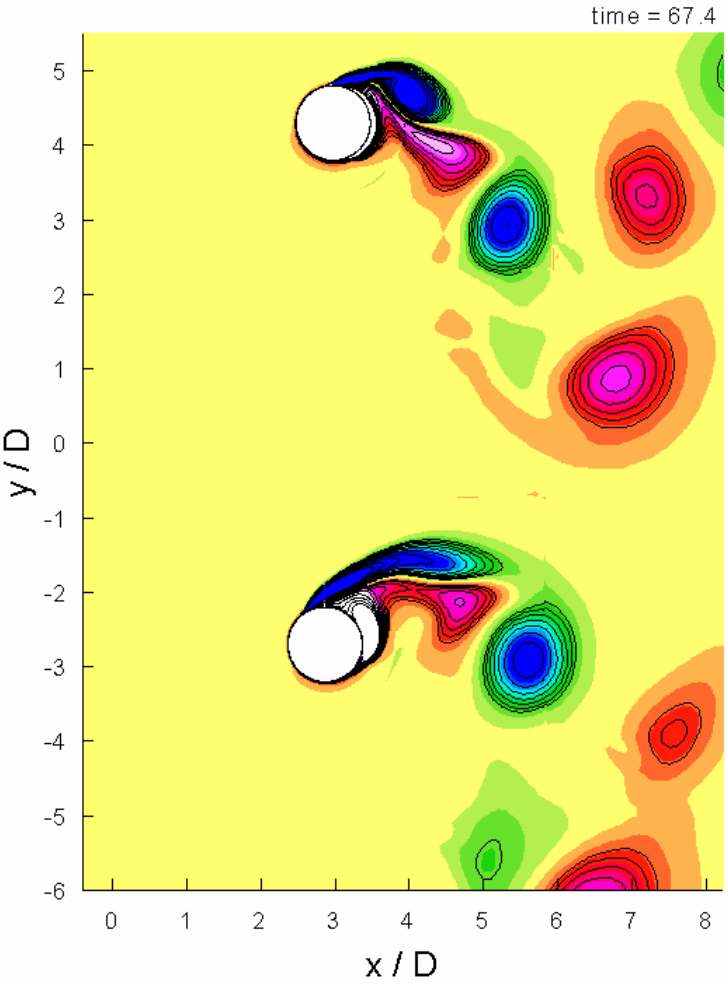


**Figure 13. Instantaneous vorticity contours depicting the in-phase VIV.**

To investigate the effects of the initial spacing between the risers, the initial center-to-center spacing was reduced to S/D = 4.5. At this initial spacing the risers first responded in anti-phase, as depicted in Figure 14. The cycle of body motion was initially a "figure-of-eight" pattern (in anti-phase), and the risers came close to each other during their half-cycle peaks. At these instants the risers came within one riser diameter (surface-to-surface) of each other. At this initial spacing, the risers repelled each other during the near-surface encounters.

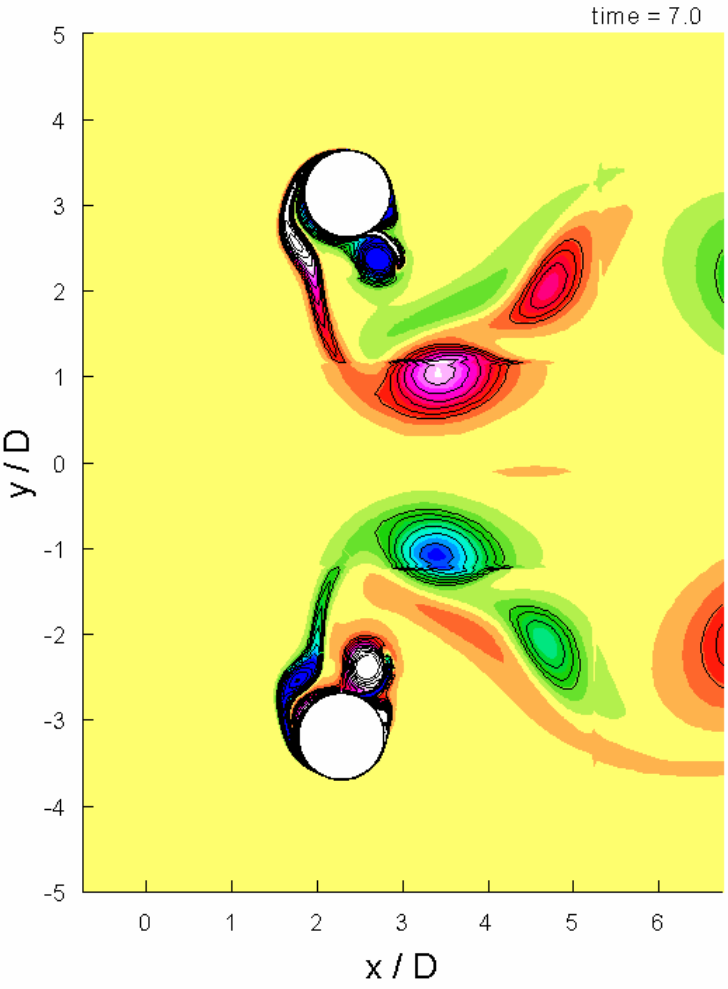


**Figure 14. Instantaneous vorticity contours depicting the anti-phase VIV.**

After several near-surface encounters, two of which are depicted in Figure 15, the "figure-of-eight" patterns distorted and eventually the risers forced each other to respond in-phase. At that point, the "figure-of-eight" patterns of body motion were restored (now in-phase) and remained stable throughout the remainder of the simulation.

We conjecture that for smaller initial gap sizes the VIV-induced forces should be strong enough to cause collisions. This was verified by performing a simulation for an initial center-to-center spacing of S/D = 4.0. The risers collided with each other, and the simulation was manually stopped due to lack of a collision model.

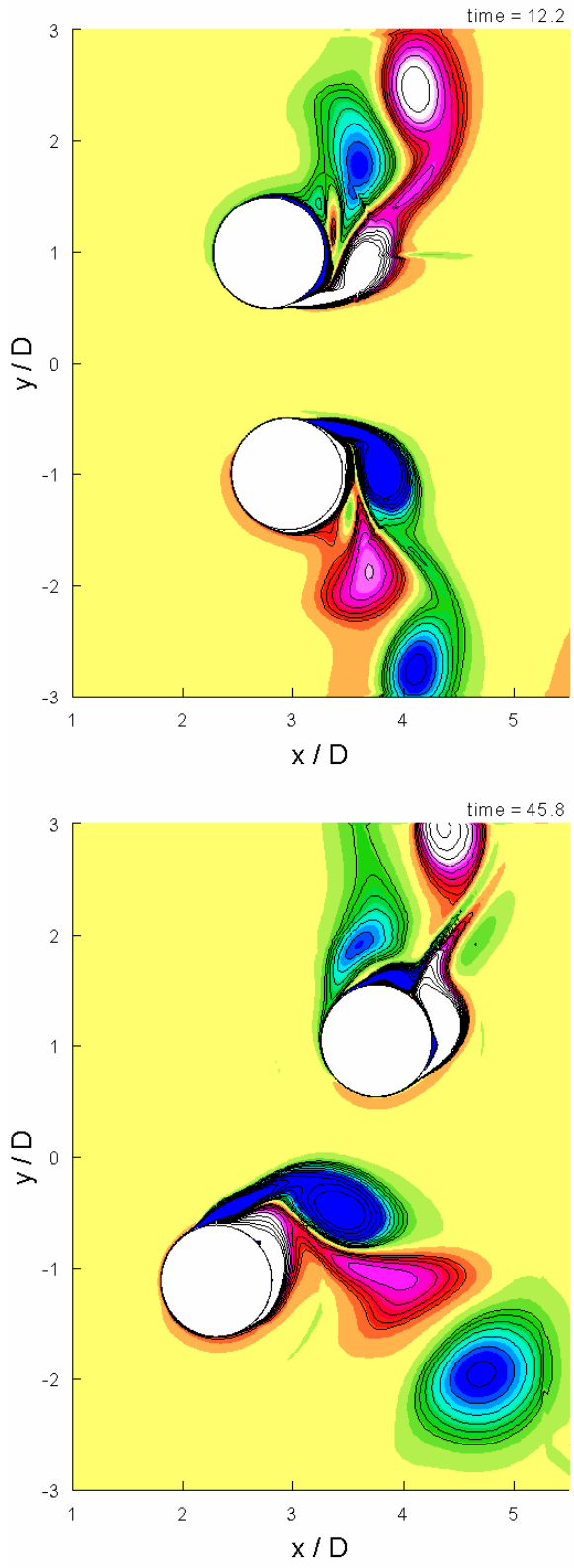


**Figure 15. Near-surface encounters in the anti-phase mode of VIV.**

These near surface encounters depict and give a clear picture of the capabilities of the overset grid approach in handling the spatial discretization around complex geometries, without the need for grid re-generation and/or mesh distortion monitoring. Even though the vorticity is post-computed independently in each grid component from the velocity field (i.e. vorticity is not made continuous across grid components), it is fairly smooth across the grid fringes. Some noise is evident at the transition to the coarse background mesh, and is due to the abrupt change in length-scale used to post-compute the vorticity.

The simulations of Blackburn et al. (2000) solve the governing equations in an accelerating reference frame, thus also avoiding the overheads of grid re-generation and/or mesh distortion monitoring. In the work of Al-Jamal and Dalton (2004) and Guilmineau and Queutey (2004) a single O-type grid is used around the riser. This approach also avoids the overheads of grid-regeneration and/or mesh distortion as the entire mesh moves together with the structure. However, these approaches may be difficult to generalize to handle VIV simulations of multiple risers with near-surface encounters, such as those depicted in Fig. 15, since the numerical grids around each riser must be deformed in order to accommodate relative motions between different risers.

### 5.4 Risers in a Square Arrangement

In addition to the interaction between two risers, it is also desirable to investigate the riser interference among four risers in a square array. This enables us to examine the interaction of multiple-risers under various ocean current orientations. To our knowledge, numerical simulations of VIV of square arrays of risers have not yet been reported or documented in the open literature. Numerical simulations of laminar vortex shedding (Re = 200) for flow past four fixed risers in two different square array arrangements were reported by Farrant et al. (2000).

Here we consider a square array of four risers with T/D = 5.5 and S/D = 5.5. Essentially, this setup corresponds to two side-by-side pairs of risers in tandem.

Once the shedding has reached full-strength for the fixed case, the risers are left free to respond to the flow field. The two upstream risers behave very much like the previously reported pair of risers in side-by-side arrangement, only this time the body motion is in anti-phase; so the two risers do come close to each other.

Figure 16 shows instantaneous vorticity contours, depicting the anti-phase motion of the two upstream risers. However, as is evident from the X-Y response plot shown in Figure 17, there is no noticeable interaction between the two upstream risers at this initial spacing.

The two downstream risers display a disorganized (non-periodic) response and experience wake-induced oscillations. Their pattern of motion is not symmetric and their

amplitude of vibration is comparable to that of the upstream risers, especially for the riser in the lower left corner of the array.

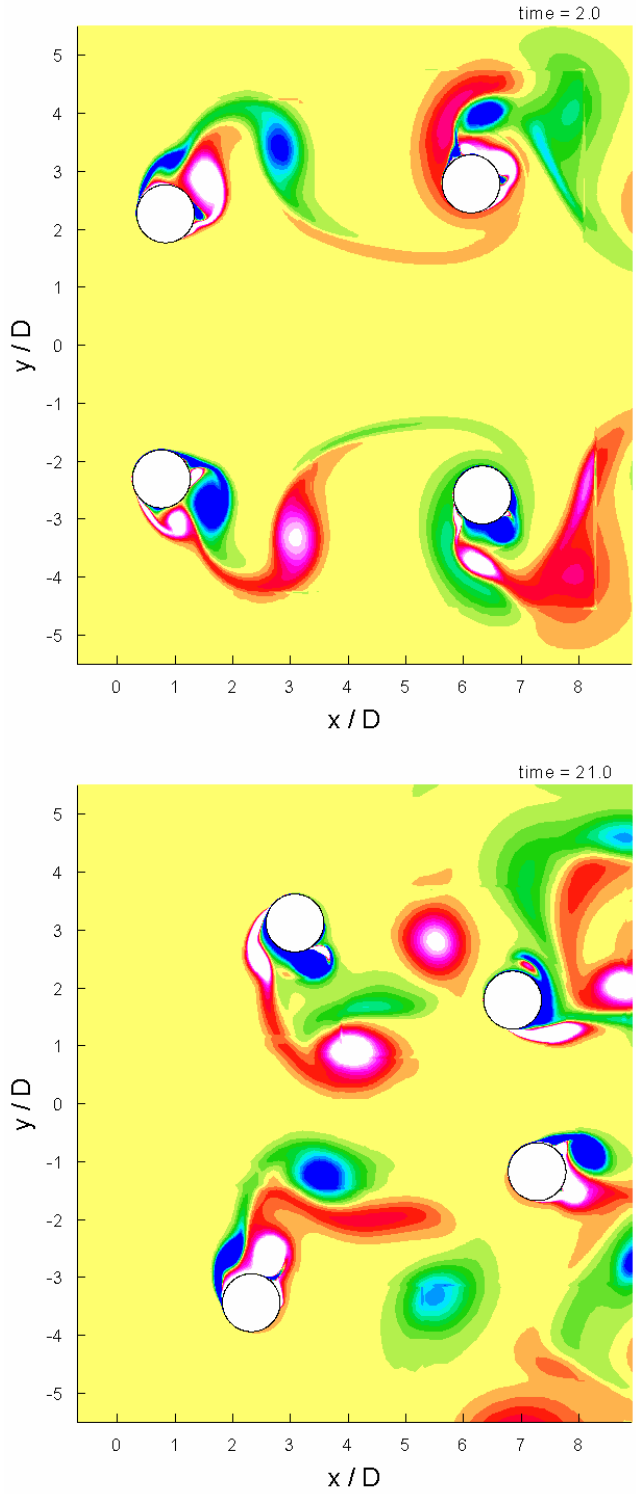


**Figure 16. Instantaneous vorticity contours for four risers in a square array arrangement undergoing VIV.**

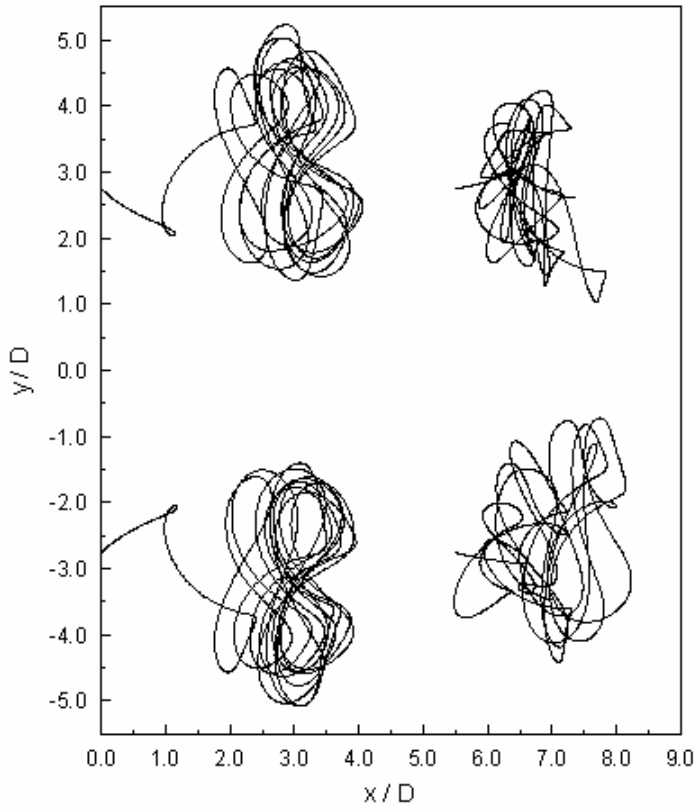


**Figure 17. X-Y response for VIV of a square array of riser.**

### 5.5 Risers in a Diamond-Shaped Arrangement

As a last example, we consider a square array of four risers with T/D = 4.0 and S/D = 4.0. The square array is rotated by 45 degrees with respect to the free-stream, to yield a diamond-shaped array. The risers are referred by numbers 1 through 4; the first one being the upstream riser of the diamond-shaped array and continuing the numbering in a counter-clockwise manner (see Figure 18).

Once the shedding has reached full-strength for the fixed case, the risers are left free to respond to the flow field. Figure 18 shows instantaneous vorticity contours of the flow field. The flow field is quite complex and noticeable interaction takes place between the risers, especially between triplets (1,2,3) and (1,4,3). Qualitatively, Riser 1 behaves like an isolated riser and has a distinguishable "figure-of-eight" pattern. Risers 2 and 4 behave like a pair of risers in side-by-side arrangement with anti-phase motion. Riser 3 experiences wake induced oscillations, as it sees the oncoming wakes from risers 1, 2, and 4. Figure 19 shows the XY-trajectory traced by the risers due to VIV.

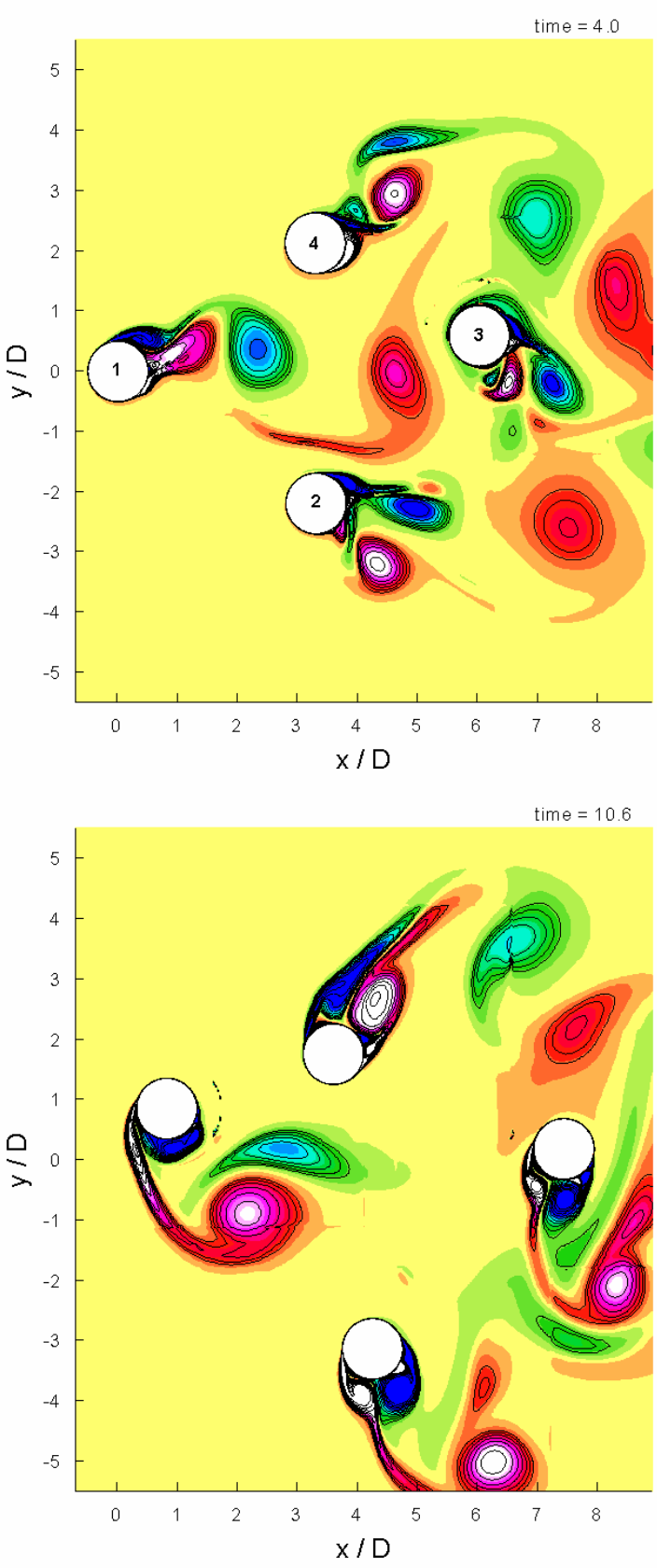


**Figure 18. VIV of four risers in a diamond-shaped array.**

Shown in Figure 19 are the trajectories during the first 50 convective time units of the fluid-induced motion. Riser 1 clearly displays a "figure-of-eight" pattern. Risers 2 and 4 are in a side-by-side arrangement, but their response is affected by the wake of riser 1. Riser 4 initially displays a "figure-of-eight" pattern, which is quickly deformed due to the oncoming irregular wake-flow.

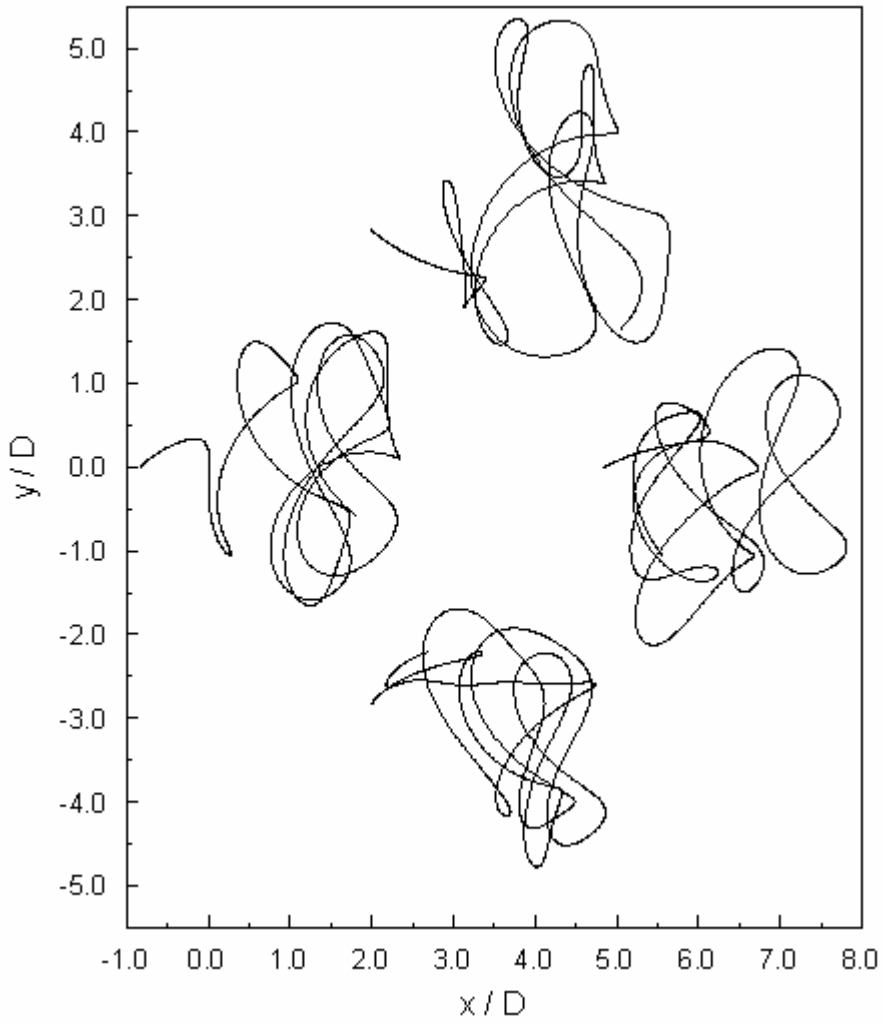


**Figure 19. X-Y-response of the diamond-shaped array for VIV; $t \in [0, 50]$.**

Similarly, shown in Figure 20 are the trajectories during the later stages of the fluid-induced motion. Riser 1 retains its "figure-of-eight" pattern, but is slightly deformed due to interactions with Riser 2, as shown. The other risers do not retain a regular pattern, but continue to experience bounded large amplitude motions.

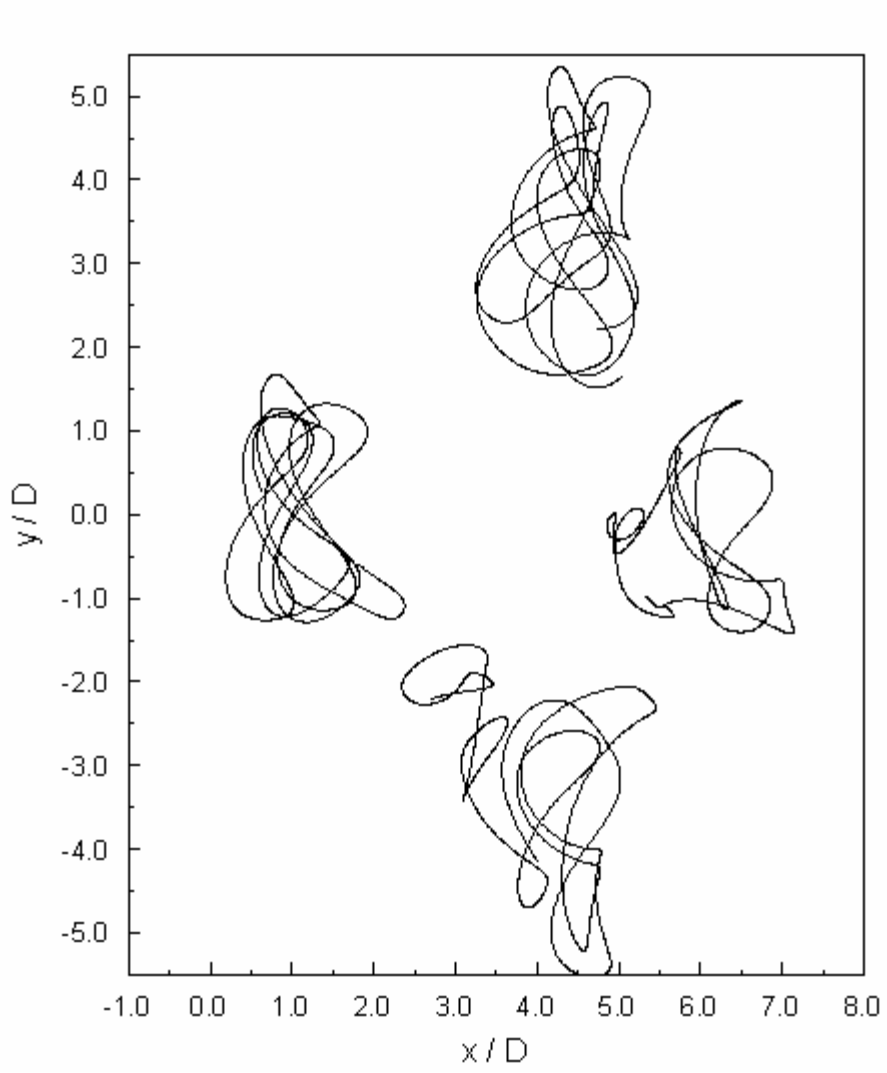


**Figure 20. X-Y-response of the diamond-shaped array for VIV; $t \in [50, 100]$.**

## 6. LES Simulations of Three-Dimensional Flow Past a Fixed Riser

Figure 21 depicts a cross-section in the X-Y plane (a "Z-slice") of the Chimera grid used for the simulations. The "Z-slice" shown has close to 35,000 cells. The cylindrical grid wrapped around the riser can be refined independently from neighboring grids to any desired level, resulting in improved local resolution and overall computational savings (as the other grid components remain un-refined).

We make further use of the Chimera technique, and allow for variable spanwise resolution within each grid component. For example, the cylindrical grid wrapped around the riser has 120 cells along its span, while the Cartesian mesh on which it is embedded has 60 cells along its span, and the far-field blocks have only 30 cells along its span.

Figure 21 also shows a spanwise cut of the grid, to show the grid distribution along the spanwise length of the riser, L/D = 3.0. In total, the mesh we use for the computations has close to 2.1 million cells.

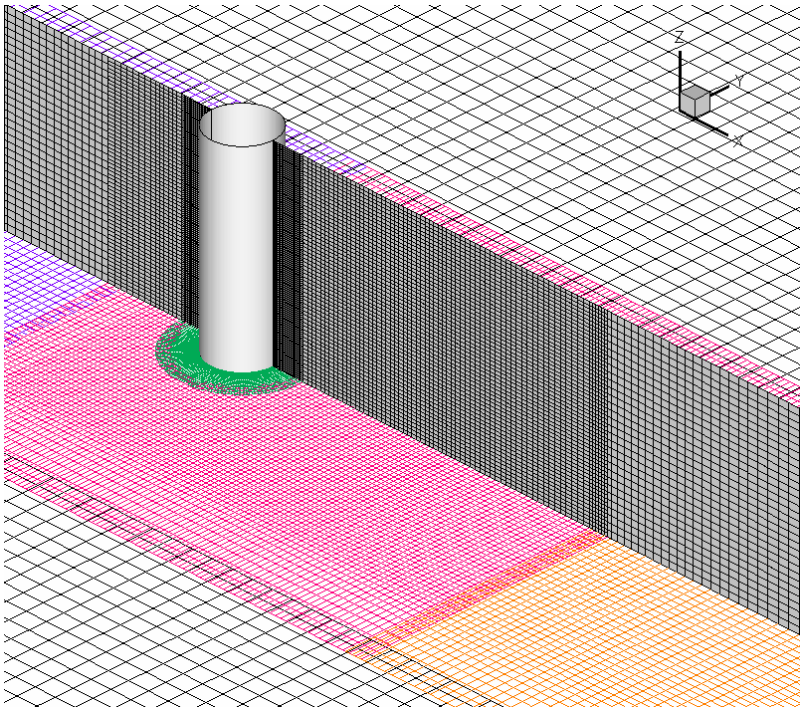


**Figure 21. Spanwise cut along Y=0.0, showing the grid distribution on the spanwise direction. Blocks in the vicinity of the riser have higher spanwise resolution.**

In the spanwise direction, we impose periodic boundary conditions. The assumption of periodic behavior in the spanwise direction is adopted to minimize the effect of the spanwise boundaries and essentially takes the spanwise direction as a

homogeneous direction. Periodic boundary conditions in the spanwise direction are normally used in large scale three-dimensional simulations of flow past a riser.

Regarding the spanwise length, taken here to be L/D = 3.0, we consider it to be sufficiently large to capture relevant spanwise wake effects. We have only access to limited computational resources, which precludes simulations with a larger spanwise length with adequate spanwise resolution.

The simulations performed in the grid shown were performed using 8 processors in parallel. Each processor was loaded with approximately 260,000 grid points. The wall-clock time per time step was around 40 seconds.

We consider the flow past a fixed riser at Re = $10^5$. In this range of Reynolds number, the only three-dimensional simulation results are those reported by Breuer (2000) at Re=$1.4\times10^5$, using LES. Still higher Reynolds numbers have been recently attempted by Catalano et al. (2003) using LES and a wall model, with not very accurate results towards the higher end of their Reynolds number range. Direct numerical simulations have been performed at Re = $10^4$ only recently by Dong and Karniadakis (2005).

As alluded to earlier, we avoid the use of any kind of wall functions, and resolve the boundary layer by using fine grid spacing near the riser surface in conjunction with the no-slip boundary condition. The near-wall spacing in the radial direction of the cylindrical grid wrapped around the riser is taken as $\Delta r/D = 10/\mathrm{Re} = 10^{-4}$, which is four times smaller than the near-wall spacing used by Breuer (2000). In all of our computations we take the Smagorinsky constant in the LES model as $C_s = 0.10$.

As expected, the flow is highly three-dimensional and unsteady, exhibiting the well-known von Karman vortex street. Figures 22a and 22b show instantaneous contours of the spanwise velocity component and of the crossflow vorticity on the center plane Y=0.0, from which the three-dimensional effects are evident. Also shown, in Figure 22c, are iso-surfaces of the streamwise vorticity component. The crossflow and streamwise vortices are generated inside the riser boundary layer and shed downstream; and exhibit a coherent structure in the spanwise direction (Figure 22b and 22c). Figure 22d shows spanwise vorticity iso-surfaces, showing a two-dimensional flow field in-front of the riser and an increasingly three-dimensional flow field downstream.

The predicted Strouhal number is St = $f_S D/V = 0.19$, where $f_S$ is the vortex shedding frequency, $D$ is the riser diameter, and $V$ is the free-stream velocity. This is in good agreement with the generally measured and accepted value of the Strouhal number St ≈ 0.20 at this Reynolds number (Bearman, 1969; Schewe, 1983). Before presenting additional comparisons with experimental data we remark that considerable scatter is present in measurements at high Reynolds numbers, due to a variety of influencing factors such as end conditions, free-stream turbulence level, and riser roughness. Nevertheless, the drawing of comparisons with experimental data is needed to establish confidence in the numerical method.

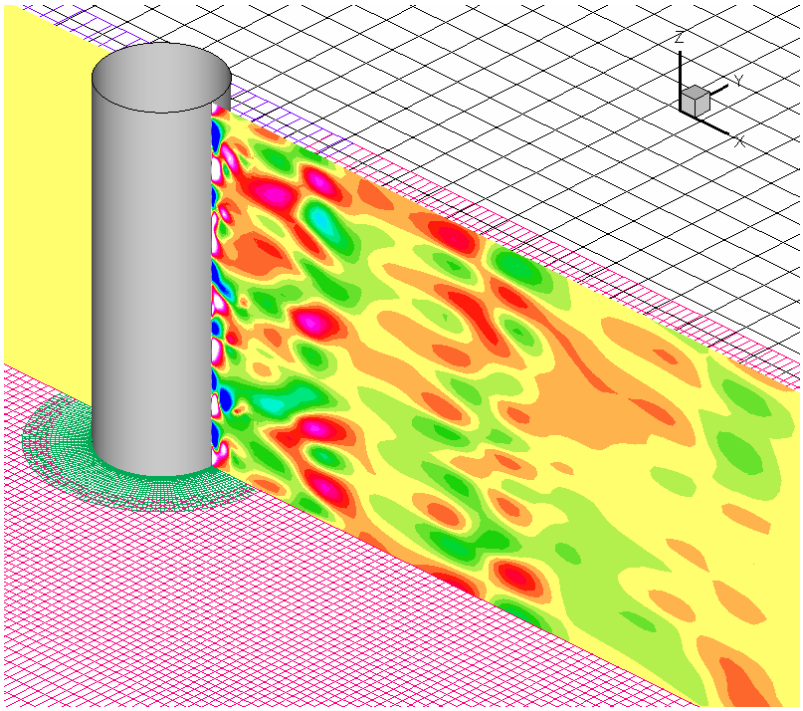

**Figure 22a. Instantaneous spanwise velocity contours for the flow past a fixed riser. Contour range [−0.2,0.2].**

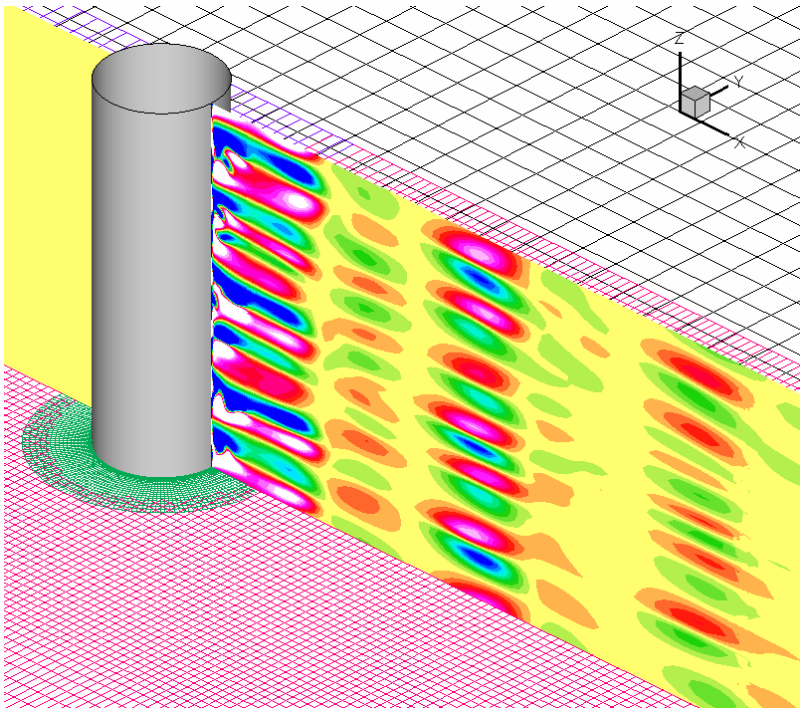

**Figure 22b. Instantaneous crossflow vorticity contours for the flow past a fixed riser. Contour range [−2,2].**

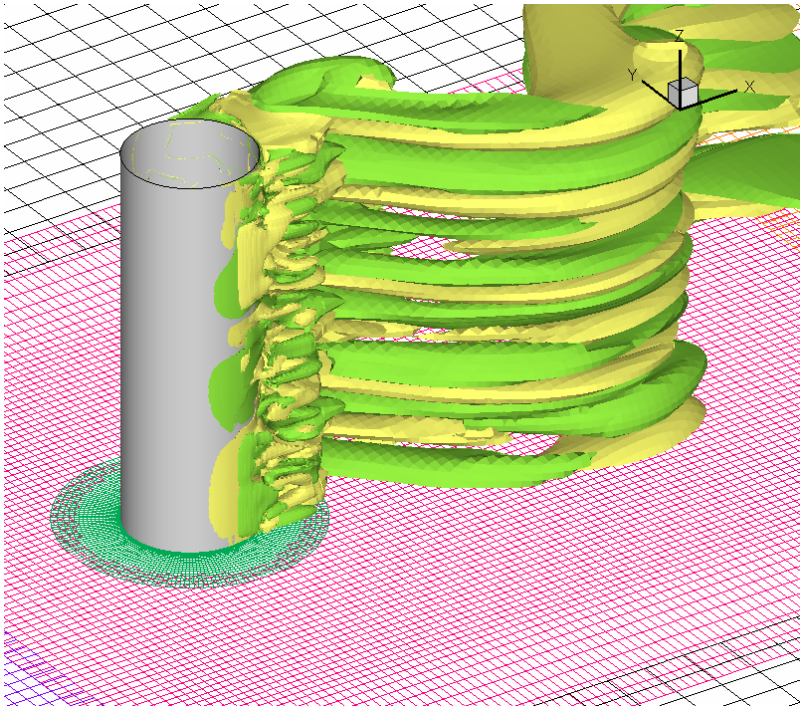


**Figure 22c. Instantaneous streamwise vorticity iso-surfaces for the flow past a fixed riser. Iso-surfaces +0.5 and −0.5.**

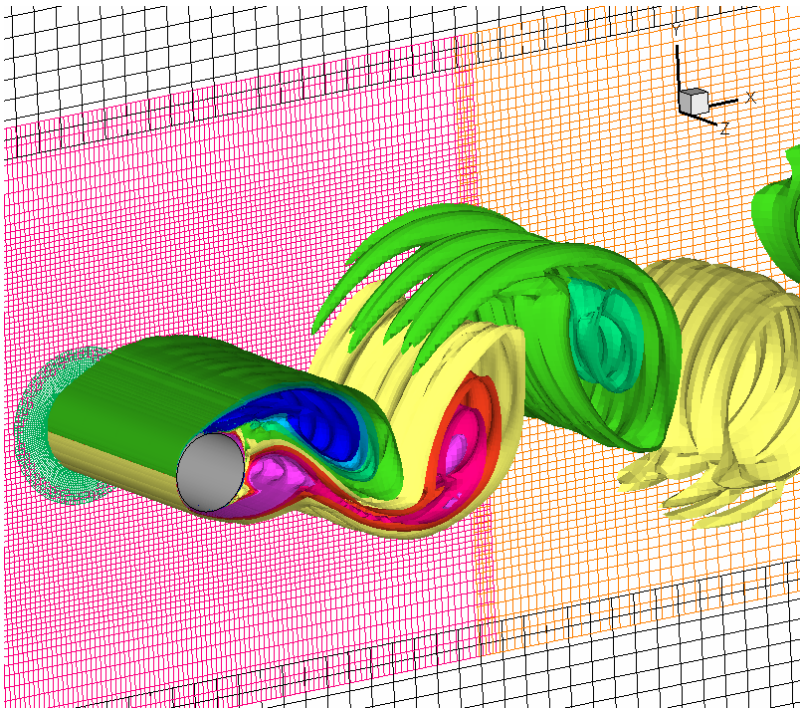


**Figure 22d. Instantaneous spanwise vorticity iso-surfaces for flow past a fixed riser. Iso-surfaces range [−4,4].**

The drag coefficient, averaged over 100 convective time units is $C_D = 1.05$. The experimental measurements of Schewe (1983) and Achenbach (1968) indicate a time-averaged value around $C_D \approx 1.20$, in fair agreement with the computed value. Simulations without the LES sub-grid model (i.e., equivalent to DNS), give a time-averaged drag coefficient of $C_D = 0.95$. Thus, we see improvement in this flow metric by using the LES model. The predicted r.m.s. lift coefficient is $C_{L,rms} = 0.62$, also in fair agreement with the measurements of Norberg (2001) with $C_{L,\,rms} \approx 0.55$.

Figure 23 shows the power spectra of the streamwise and crossflow velocities at two points in the near wake of the riser, on the plane Z=1.5. The spectra of the crossflow velocities have a peak at the Strouhal number frequency $f_S$ (St = $f_S D/V$). The small and some medium scales are being suppressed due to insufficient grid resolution, as the grid cut-off frequency occurs around 1.0. Additional mesh refinement would be needed to adequately resolve these scales. Nevertheless, the large energy content of the spectra is resolved and the grid cut-off takes place after the energy has dropped by four orders of magnitude. The spectra qualitatively follow the −5/3 slope in the resolved part of the inertial subrange, which is a fundamental theoretical result for isotropic turbulence in three-dimensions.

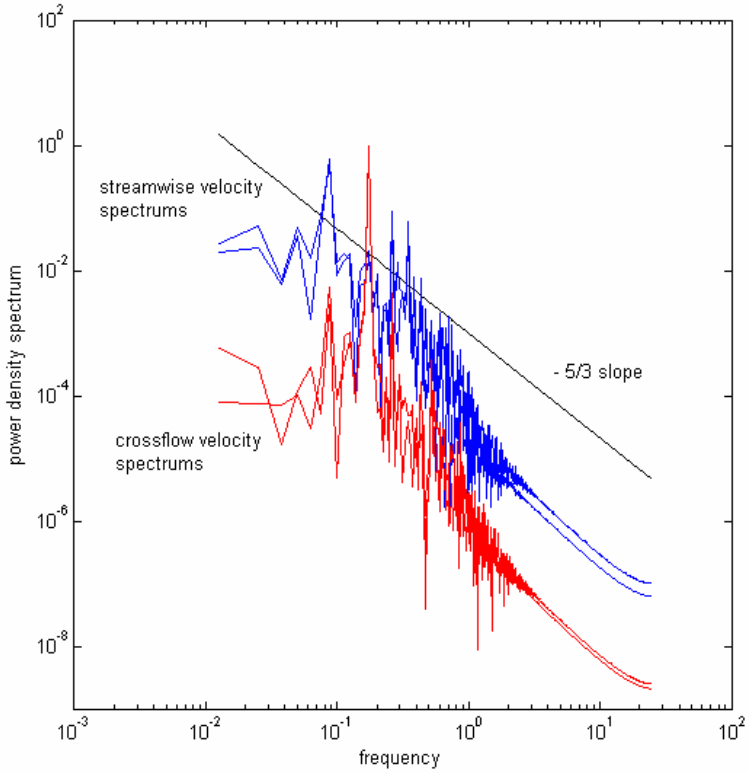


**Figure 23. Power spectra of streamwise and crossflow velocities in the near wake of the riser.**

.

# 7. LES Simulations of Three-Dimensional Flow Past an Elastically Mounted Riser Undergoing VIV

We are interested in the structure's response for low mass and damping. The values for the mass ratio, damping ratio, and reduced velocity used for the simulations in this study are: $m^*$=1.0, $\zeta^*$= 0.005 and $U^*$ = 6.055.

The riser is first held fixed until the shedding has reached full strength, at which point the riser is "released" and allowed to respond to the flow field. Figure 24 shows the X-Y response of the riser for 100 convective time units, where time is implicit in the plot.

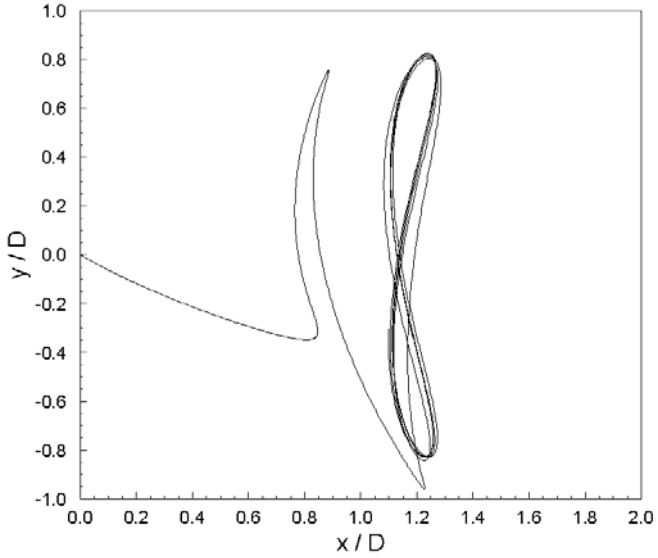


**Figure 24. X-Y trajectory swept by the riser due to VIV. The response is a "figure-of-eight" pattern of body motion.**

Initially the riser is pushed downstream due to the acting drag force exerted by the oncoming fluid. Almost immediately, the riser responds to the acting lift forces and starts displaying strong cross-stream oscillations. Once the pattern of motion has settled, the X-Y response displays average peak-to-peak cross-stream amplitudes of 1.65 riser diameters. There is also weak in-line motion with average peak-to-peak amplitudes of 0.160 riser diameters. The response is remarkably stable and corresponds to a "figure-of-eight" pattern which was maintained throughout the simulation time of 250 convective time units.

Analysis of the power spectrum of the time history of body motion gives $f_X$ / $f_Y$ = 2.0, i.e. the streamwise oscillation frequency is twice that for the transverse (cross-stream) direction. In addition, we continue to find that a good representation of the average displacement pattern in the simulation is given by

$$y(t) = A_Y \sin(\omega t) \qquad x(t) = A_X \sin(2\omega t + \theta)$$

where $A_Y$ is the average cross-stream amplitude of vibration, $A_X$ is the average streamwise amplitude of vibration, $\omega = 2\pi f_Y$, and $\theta$ is the phase angle. The following coefficients were extracted from the predicted time history response of our simulation: $A_Y = 0.824$, $A_X = 0.0795$, $f_Y = 0.1757$, and $\theta = -40°$.

In an experimental study, Jeon and Gharib (2001) forced a riser to move in the X and Y direction according to the above equations as they suggested that nature prefers the "figure-of-eight" patterns. Our simulations, confirm that this is indeed the case. As noted in Jeon and Gharib (2001), the large transverse motion sets the frequency of shedding, but the phase of the wake can be strongly affected by the phase of the streamwise motion. Changing the relative phase of shedding not only alters the phase of lift force, but may also change the direction of energy transfer between the body and the wake. They further noted that a relatively small streamwise motion can have profound effects on the wake by changing the surface acceleration to the circulation production. Since the streamwise motion is at twice the frequency of the transverse motion, its contribution to acceleration is quite comparable to that due to the transverse motion even though the amplitude of streamwise motion is much smaller. For an unconstrained riser, the combined effects of phase change and circulation production due to streamwise motion tend to produce a two degree-of-freedom VIV motion with stable figure-of-eight pattern as shown in the present simulations.

We believe the response falls towards the start of the recently discovered "super-upper" branch (Jauvtis and Williamson, 2004) for light bodies ($m^* < 6.0$) undergoing two-degree-of-freedom VIV. Although the experiments of Jauvtis and Williamson (2004) were conducted at lower Reynolds numbers ($Re = 10^3 - 10^4$), the predicted response clearly displays the high cross-stream amplitudes associated with this branch.

Unlike our previous two-dimensional simulations, where the 2T mode of vortex shedding was observed (see Section 5.1), here we see a 2S mode of vortex shedding. In this mode, the riser sheds two single vortices per cycle of body motion, whereas in the 2T mode two triplets of vortices are shed per cycle of body motion.

Figure 25 shows instantaneous spanwise vorticity contours on the XY plane corresponding to the spanwise location Z=1.5, showing the 2S mode of vortex shedding. The figure depicts the riser at the bottom and half-cycle of body motion. We conjecture that the 2T mode will be seen at higher reduced velocities, as one climbs the super-upper branch and the cross-stream amplitudes of vibration increase in magnitude.

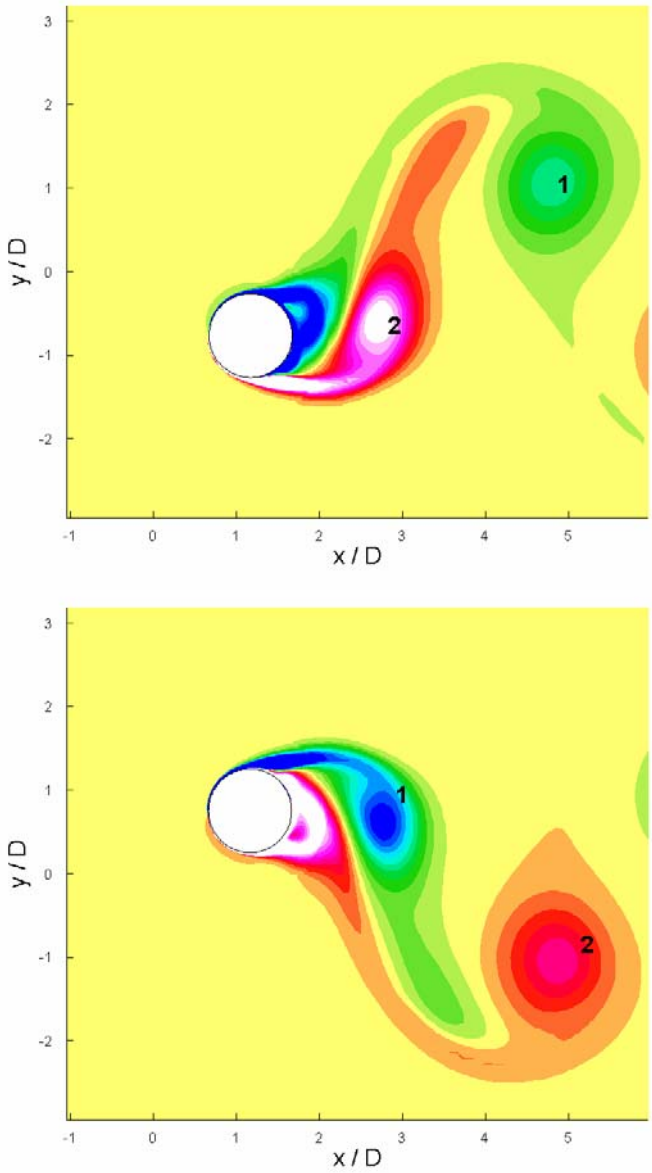


**Figure 25. Spanwise vorticity contours on the X-Y plane Z=1.5, showing the 2S mode of vortex shedding.**

Our previous two-dimensional numerical simulation results, at the same flow and structural conditions, display much stronger cross-stream and streamwise amplitudes of vibration: $A_Y$ = 1.54, $A_X$ = 0.54 (see Section 5.1). However, due to the omission of spanwise wake effects in the two-dimensional simulations; the oscillatory lift forces are much stronger. Consequently, the cross-stream amplitudes of vibration are nearly double and the streamwise amplitudes nearly seven times larger than those seen here for the three-dimensional case. This indicates that three-dimensional effects are important and contribute significantly to the VIV response. A comparison of the motion amplitudes and time-averaged drag coefficients for the two- and three-dimensional cases are given in Table 1.

**Table 1. Comparison of motion amplitudes, frequencies, phase angle, and drag coefficients between 2D and 3D simulations.**

| | 2D | 3D |
|---|---|---|
| Cross-stream Amplitude $A_Y$ | 1.54 | 0.824 |
| Streamwise Amplitude $A_X$ | 0.54 | 0.0795 |
| Cross-stream Frequency $f_Y$ | 0.14 | 0.1757 |
| Streamwise Frequency $f_X$ (=2$f_Y$) | 0.28 | 0.3514 |
| Phase Angle $\theta$ | –18° | –40° |
| Time-Averaged Drag Coefficient $C_D$ | 5.20 | 2.02 |

The flow field remains highly three-dimensional during VIV. Figure 26 shows spanwise vorticity iso-surfaces at an instant in the "figure-of-eight" cycle of motion when the riser's crossflow velocity is maximum and the riser is moving (upward) in the positive Y direction. The 2S mode of vortex shedding is also clearly visible from this plot.

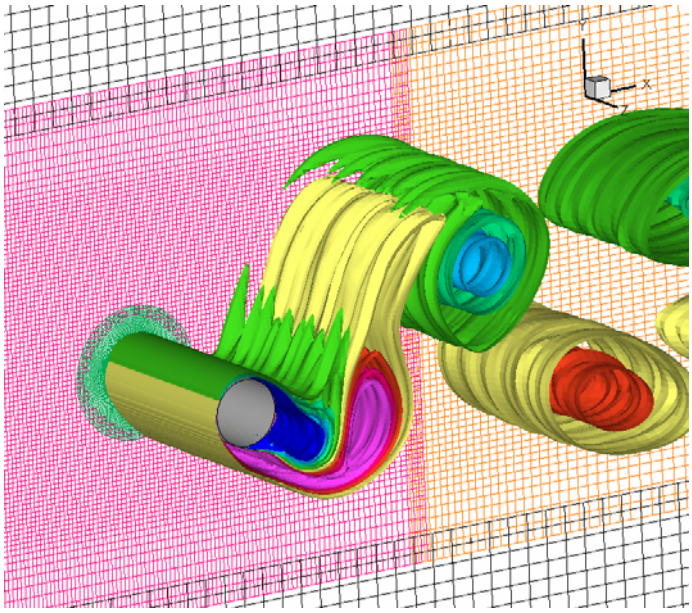

**Figure 26. Instantaneous spanwise vorticity iso-surfaces for two degree-of-freedom VIV of a 3D riser. Iso-surfaces range [−4,4].**

Figure 27 shows the time history of the transverse displacement, the lift coefficient, and the corresponding phase plot. Our simulations show that despite the fact that the fluid-induced forcing is non-sinusoidal (it has higher harmonics); the displacement remains remarkably close to sinusoidal. In order to obtain a better understanding of the fluid-structure interactions between the non-sinusoidal lift force and

the sinusoidal displacement, it is desirable to analyze the detailed three-dimensional velocity and pressure data over several shedding periods. Due to the enormous storage requirements, however, we did not attempt to save a complete set of 3D velocity and pressure data to facilitate an in-depth analysis of the observed lift and drag forces. When more computer resources become available in the future, it will be worthwhile to investigate the effects of 3D vortex shedding on the fluid forces and the corresponding riser motions in order to improve our understanding of the fluid-structure interactions for 3D risers.

An increase in the drag coefficient is observed, with a time-average drag of $C_D$ = 2.02. Compared to the fixed case, the mean drag is doubled. The phase plot of the drag and lift coefficients in Figure 28 exhibits an interesting shape. The plot depicts the strong periodicity of the flow induced forces.

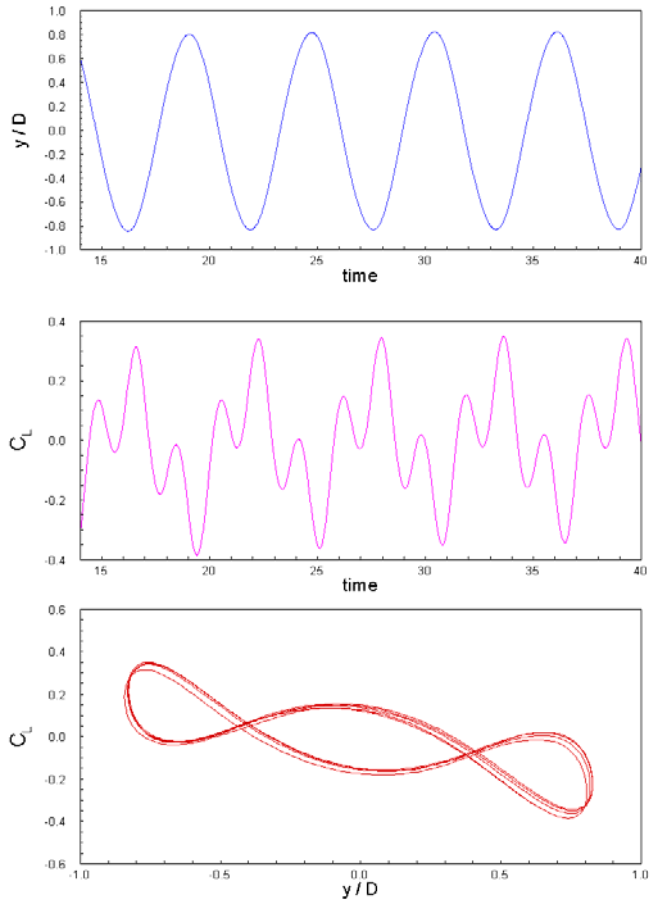


**Figure 27. Time histories of transverse (cross-stream) displacement and lift coefficient. We also show the corresponding phase plot.**

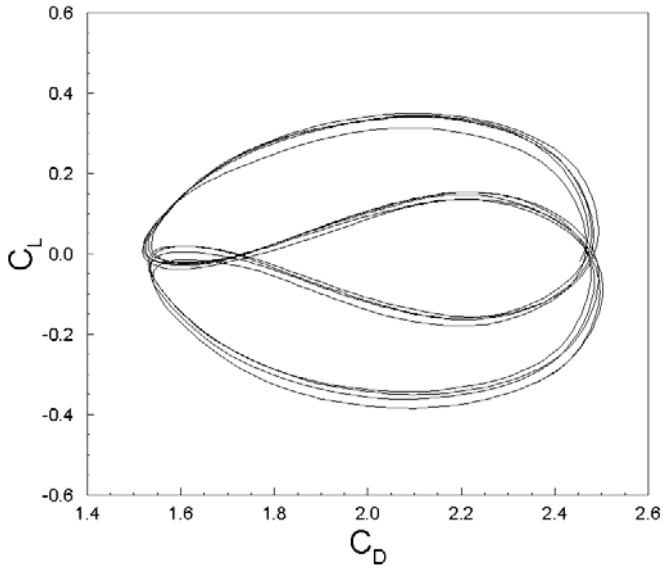


**Figure 28. Phase plot of the drag and lift coefficients. Average and fluctuating values can be obtained from the plot.**

The power spectrum of the time history of the lift coefficient is shown in Figure 29. The frequency is scaled by the first fundamental frequency, and we see that there is a strong higher harmonic at three times the first fundamental frequency. The excitation of the 3× harmonic is typical of responses in the super-upper branch, although we did not see the 2T mode of vortex shedding at this reduced velocity.

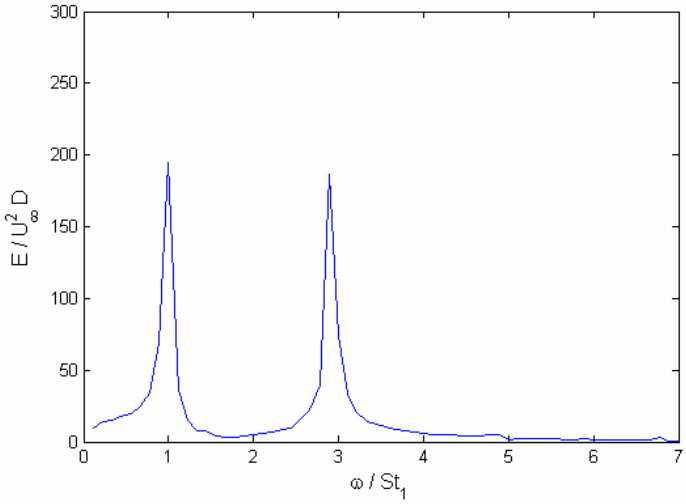


**Figure 29. Power spectrum of the time history of the lift coefficient, showing a strong 3× harmonic.**

## 8. Simulations of an Elastically Mounted Riser Outfitted with a Fairing

Figure 30 shows a close-up view of the Chimera grid around the riser when it is outfitted with the fairing. The different block-structured components are shown in different colors. Also shown is a close-up view of the grid around the tail of the fairing. The individual grid components around the fairing can be refined independently from neighboring grid components, resulting in improved local resolution and overall computational savings (as the other grid components remain un-refined). The grids shown in Figure 30 are embedded in still coarser background grids, as shown in Figure 31, to represent the far-field.

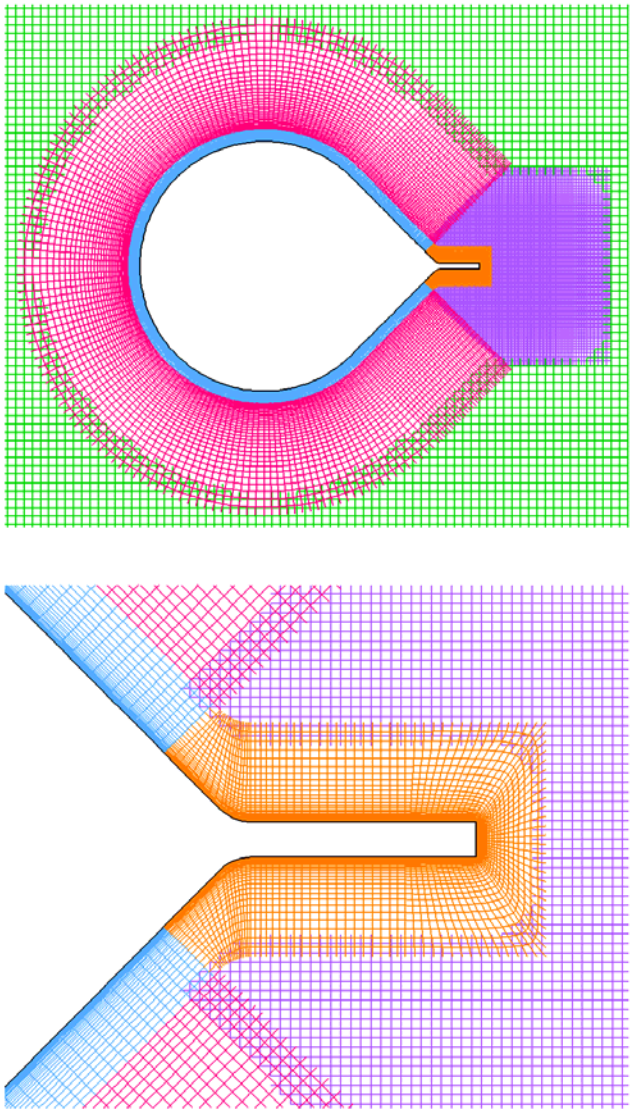

**Figure 30. Close-up views of the overset (Chimera) grid for VIV of a riser outfitted with a fairing.**

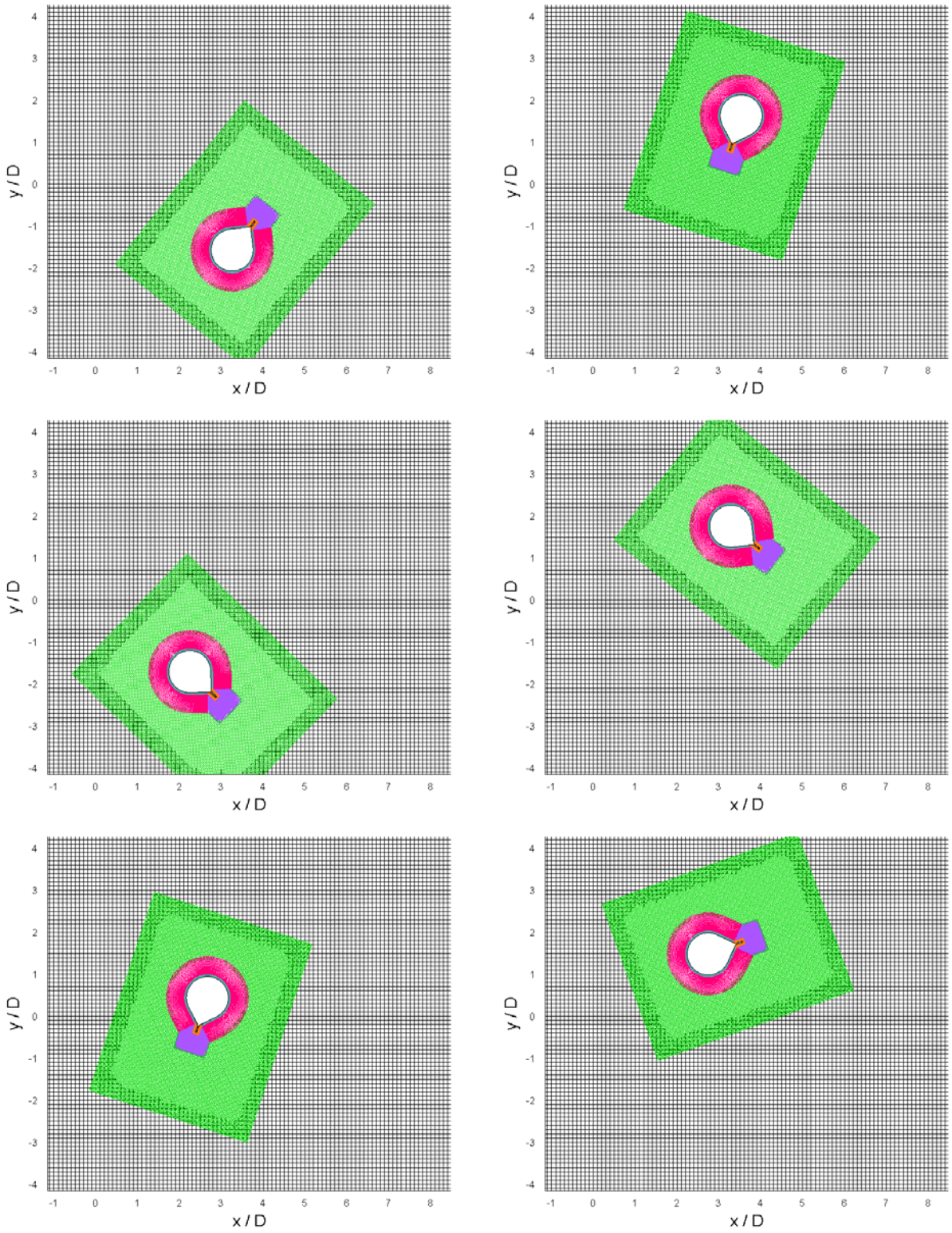


**Figure 31. Snapshots of the Chimera grid in time (top to bottom), during three-degree-of-freedom (X,Y,θ) motion.**

We avoid the use of any kind of wall functions, and resolve the boundary layer by using fine grid spacing around the fairing surface in conjunction with the no-slip boundary condition. The near-wall spacing in the normal direction of the grid wrapped around the fairing is taken as $\Delta r/D = 10/Re$. This gives a near wall spacing of $10^{-4}$ and $10^{-5}$ for the two Reynolds numbers considered in this study, respectively. In terms of wall coordinates, the grid maintains a near-wall spacing of $y^+ \leq 0.20$ for the Reynolds numbers considered. The fine grid spacing around the surface of the fairing can be appreciated from Figure 30. Overall, the grid has a total of 81,000 grid points. The simulations performed in the grid shown were executed using 4 processors in parallel. Each processor was loaded with approximately 20,000 grid points.

When the outfitted riser undergoes three-degree-of-freedom VIV, the meshes shown in Figure 30 move on top of earth-fixed background Cartesian meshes, thus avoiding tedious grid-regeneration and/or mesh distortion monitoring. The interpolation stencils that are needed to communicate across grid components are simply updated as the grid moves. Snapshots of the Chimera grid during three-degree-of-freedom VIV motion (for zero torsional stiffness) are shown in Figure 31 to give the reader a clear idea of the capabilities of the Chimera grid approach.

When given the freedom of angular motion, the structure's angular response is assumed to be governed by an equation of the form

$$J^* \ddot{\theta} + b^* \dot{\theta} + \kappa^* \theta = \frac{2}{\pi} C_M(t)$$

where the dimensionless moment of inertia $J^* = m^*/8$ for a uniform disk, the dimensionless torsional damping is set to zero $b^* = 0.0$, and we vary the dimensionless torsional stiffness $\kappa^*$ to achieve maximum VIV suppression. We are interested in the structure's response for low mass and damping. The values for the mass ratio, damping ratio, and reduced velocity used for the simulations in this study are: $m^*=1.0$, $\zeta^* = 0.005$ and $U^* = 6.055$.

### 8.1 LES Simulation at Re = $10^5$

Once the riser is outfitted with the fairing we find that the amount of VIV suppression is sensitive to the value of the torsional stiffness, $\kappa^*$, of the structure. Figure 32 shows the instantaneous vorticity contours for the fairing-outfitted riser with four different torsional stiffness values of $\kappa^* = 0$, 0.10, 0.50, and $\infty$ (i.e., fixed, no rotation allowed). The simulation results indicate that the fairing tends to increase the VIV amplitude for the extreme cases with either zero or very large torsional stiffness. On the other hand, a torsional stiffness of $\kappa^* = 0.5$ was found to be very effective in suppressing the VIV response as seen in Figure 32(c). It should be remarked that the optimal $k^*$ and $b^*$ may vary significantly with the mass ratio, structural damping ratio, reduced velocity, and Reynolds number. Therefore, no attempt has been made in the present study to find the optimal torsional stiffness $\kappa^*$ or torsional damping $b^*$.

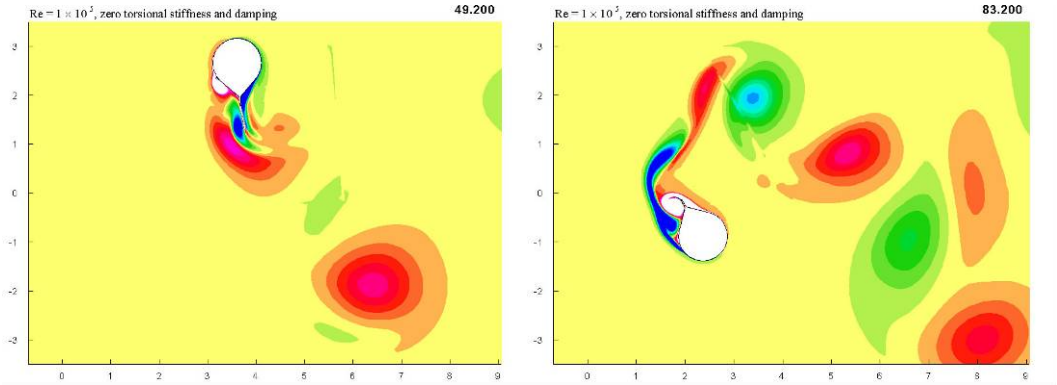


**(a)** $b^* = 0$, $\kappa^* = 0$

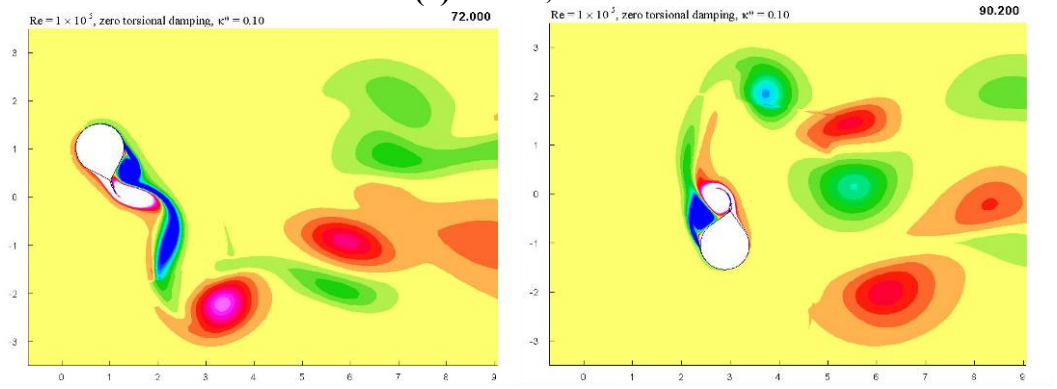


**(b)** $b^* = 0$, $\kappa^* = 0.10$

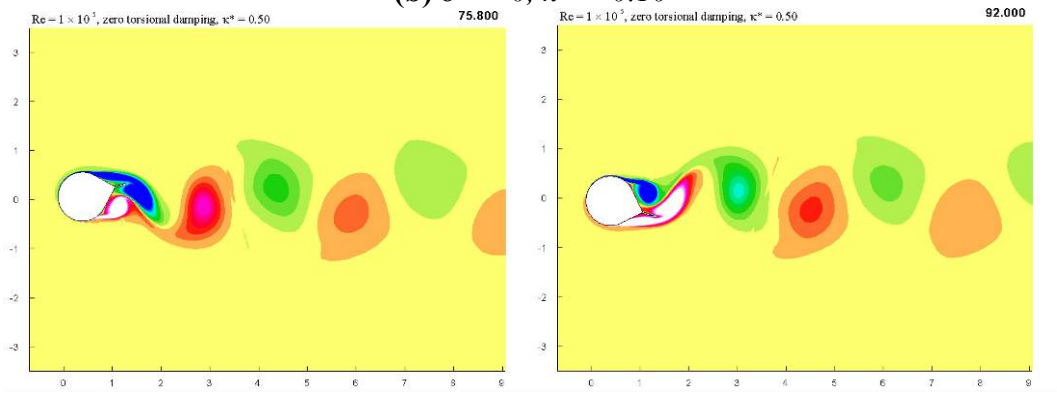


**(c)** $b^* = 0$, $\kappa^* = 0.50$

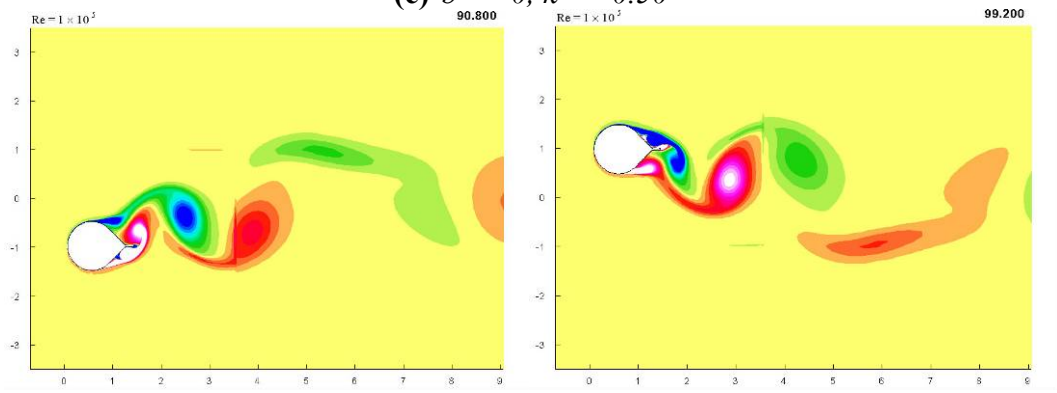


**(d)** $b^* = 0$, $\kappa^* = \infty$

**Figure 32. Vorticity contours for VIV of a fairing-outfitted riser.**

Figure 33 shows the X-Y response of the fairing-outfitted riser for torsional stiffness $\kappa^* = 0.50$, Re = $10^5$, and $t \in [0, 100]$, where time is implicit in the plot. For direct comparison we also plot the response of the bare riser. Clearly, we see significant VIV suppression.

The amount of VIV suppression may be quantified by comparing the cross-stream displacement time history for the bare and outfitted risers, also shown in Figure 33. We see that the outfitted riser gives slightly over 60% VIV suppression in this measure.

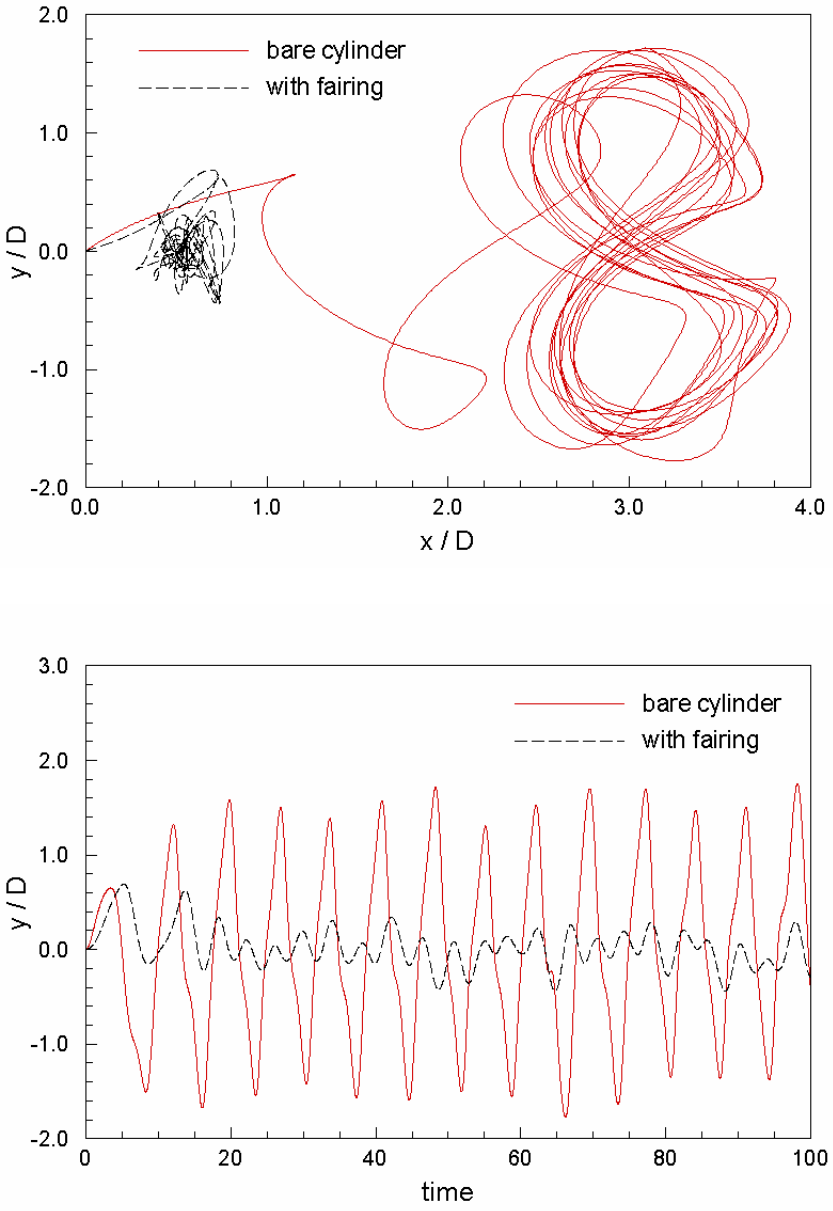


**Figure 33. X-Y trajectory and time history of cross-stream displacement for the bare and faring-outfitted riser, Re = $10^5$.**

We observe from animations of the simulations that the VIV suppression is brought about by the rapid "wagging" of the fairing tail, and thus the VIV suppression is directly related to the torsional spring-back of the fairing. Figure 34 shows the time history of the angular displacement of the outfitted riser. The frequency associated with the angular motion is $f_\theta = 0.250$, with an average amplitude of 31.5 degrees.

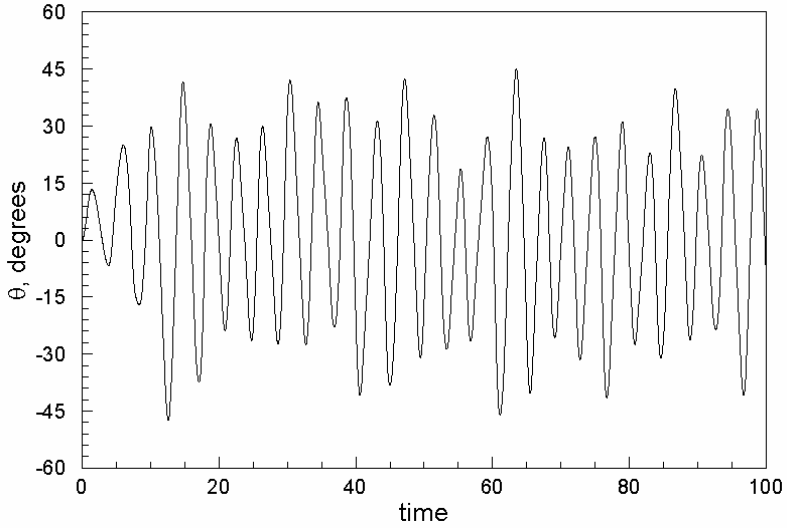


**Figure 34. Time history of the angular displacement due to the fluid-induced moment on the fairing-outfitted riser, Re = $10^5$.**

Comparisons of time histories of the drag and lift coefficients on the bare and outfitted risers are shown in Figure 35. We observe a significant decrease in the drag coefficient and the amplitude of the lift coefficient for the fairing-outfitted riser.

The VIV will continue to be further suppressed with increasing values of $\kappa^*$, up to a critical value at which point the VIV will commence to increase as shown earlier in Figure 32. Too much torsional stiffness will prevent the structure from rotating, thus eliminating the mechanism by which VIV suppression is made possible.

In closing the LES subsection, we note that the grid spacing used around the bare and outfitted risers was such that the eddy viscosity in these areas was negligibly small (i.e. less than $1/\text{Re} = 10^{-5}$ when checked in the post-processing stage). This simply means that the grid spacing in these areas was small enough to adequately resolve medium to small eddy scales. Simulations without the LES model gave nearly identical results in instantaneous drag, lift, and moment coefficients – and consequently the VIV response.

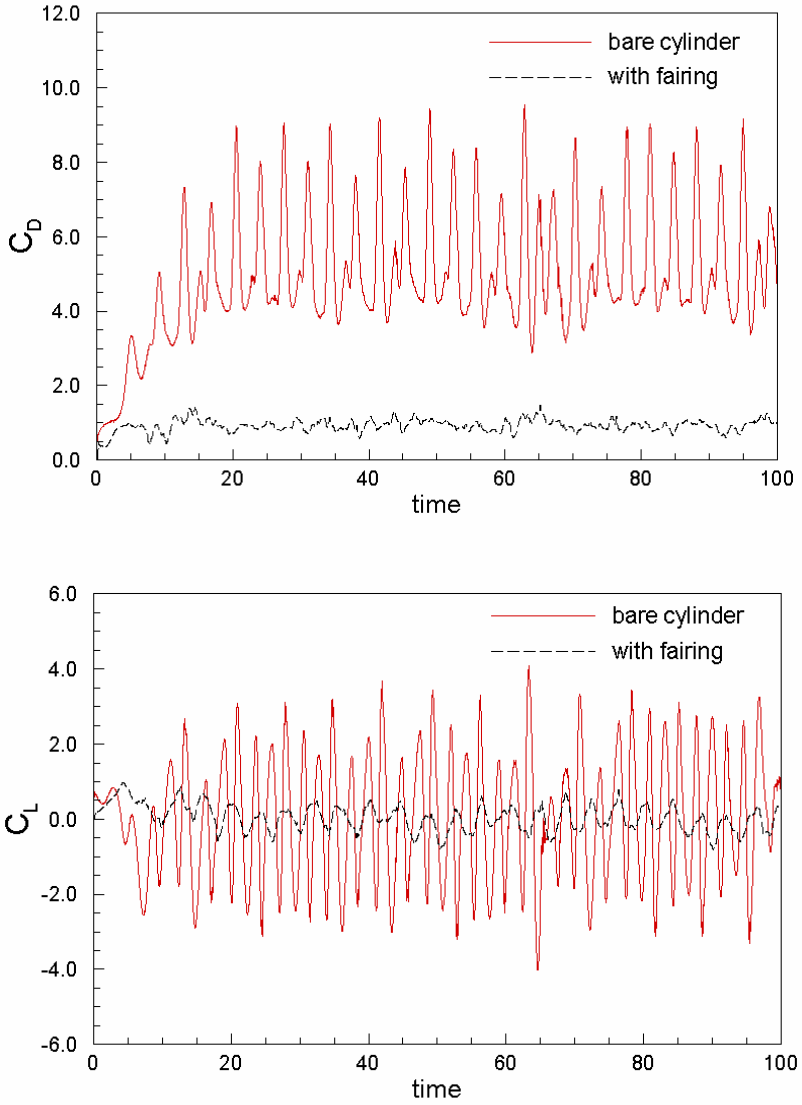


**Figure 35. Time history of drag and lift coefficients for the bare and faring-outfitted riser, Re = $10^5$.**

### 8.2 RANS Simulation at Re = $10^6$

The X-Y response of the bare and outfitted risers due to VIV at Re = $10^6$ is shown in Figure 36. The bare riser displays average peak-to-peak cross-stream amplitudes of 2.8 riser diameters, with weak in-line motion having peak-to-peak amplitudes of 0.15 riser diameters.

As is evident from Figure 36, the response computed using the RANS equations is much more periodic than that observed for the LES. This is due to the ensemble-averaging of the Navier-Stokes equations and the modeling of the fluctuating components in the RANS.

Like before, computations for the fairing-outfitted riser were performed using a torsional stiffness value of $\kappa^* = 0.50$. Significant VIV suppression is observed. Comparing the cross-stream displacement time history for the bare and outfitted risers, also shown in Figure 36, we see that the outfitted riser gives slightly over 90% VIV suppression in this measure.

The time history of the angular displacement of the fairing-outfitted riser is shown in Figure 37. The frequency associated with the angular motion is $f_\theta = 0.260$, with an average amplitude of 22.5 degrees.

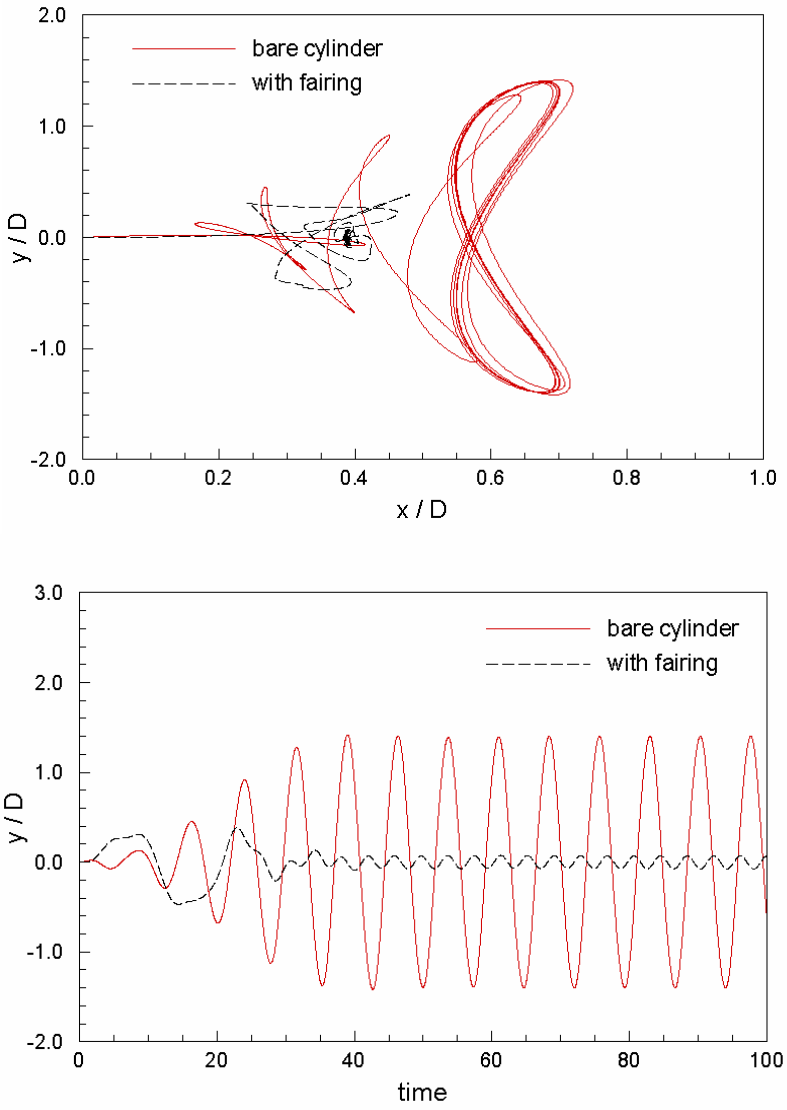


**Figure 36. X-Y trajectory and time history of cross-stream displacement for the bare and faring-outfitted riser, Re = $10^6$.**

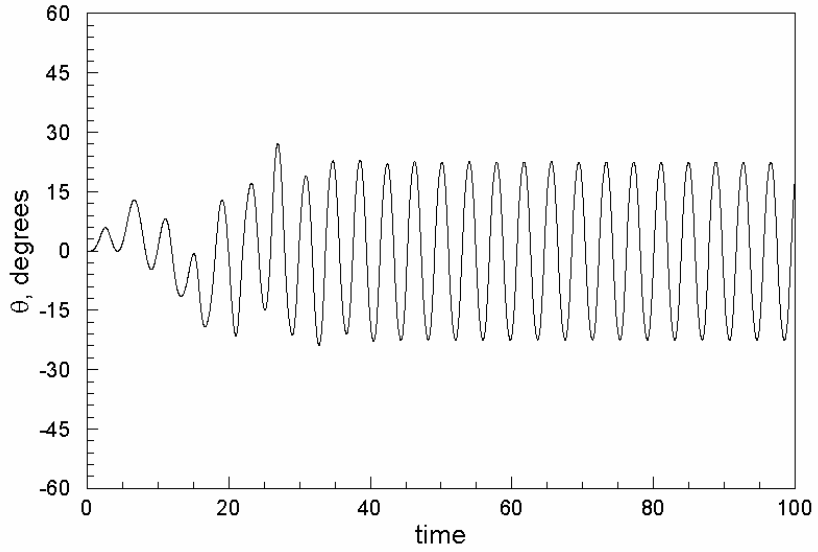


**Figure 37. Time history of the angular displacement due to the fluid-induced moment on the fairing-outfitted riser, Re = $10^6$.**

## 9. Simulations of an Elastically Mounted Riser with Helical Strakes

Figure 38 shows a spanwise cross-section of the overset grid used for the straked riser simulations. We use a single body-fitted structured grid around the straked surface, as shown. The geometry corresponds to a generic helical strake with 3 protruding triangles spaced 120 degrees from each other and having a spanwise pitch of 9 riser diameters. The Chimera grid for the straked riser has the same block structure as that shown earlier in Figure 21 for the bare riser. The boundary-fitted grid wrapped around the straked riser has 120 cells along its span, while the Cartesian mesh on which it is embedded has 60 cells along its span, and the far-field blocks (not shown) have only 30 cells along its span. We performed full 3D simulation for a single pitch, and use periodic boundary conditions along the span of the straked riser. The Reynolds number is Re = $10^5$.

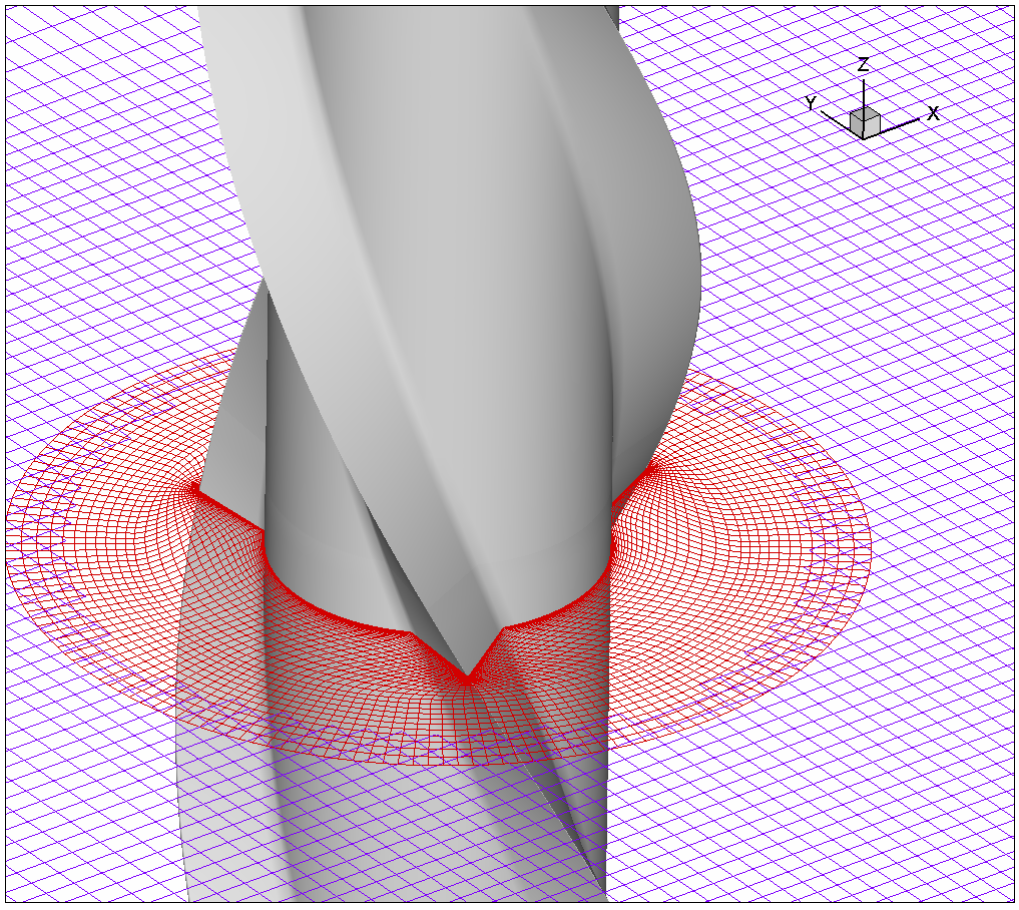


**Figure 38. Spanwise cross-section of the overset grid for flow past a straked riser.**

The intent of the helical strakes is to prevent a single dominant shedding frequency from occurring. As shown in Figures 39 and 40 (for the fixed case), this is achieved by altering the flow separation along the span and by preventing the interaction of the shear layers close to the base of the riser. Figure 39 shows instantaneous pressure contours, illustrating the non-uniform separation of the flow along the span. For fixed bare risers, the thin shear layer always develops from the stagnation line at the leading edge ($\theta$ = 0°) as shown in Figure 22d and separates from the body surface at approximately the same angular position in the spanwise direction (i.e., two-dimensional separation). For the straked riser, the stagnation line intercepts the strakes at three different positions within a single pitch as shown in Figure 39. This leads to the development of a highly three-dimensional shear layer along the straked surface. At each spanwise location, the 3D shear layer developed from the stagnation line is further disrupted by the downstream strakes at different angular positions. It is clearly seen from the spanwise vorticity contours shown in Figure 40 that the shear layer separates along the sharp tip of the helical strakes at different angular positions in the spanwise direction. This alters the phase angle of the vortex shedding patterns along the span and prevents the development of a single dominant shedding frequency.

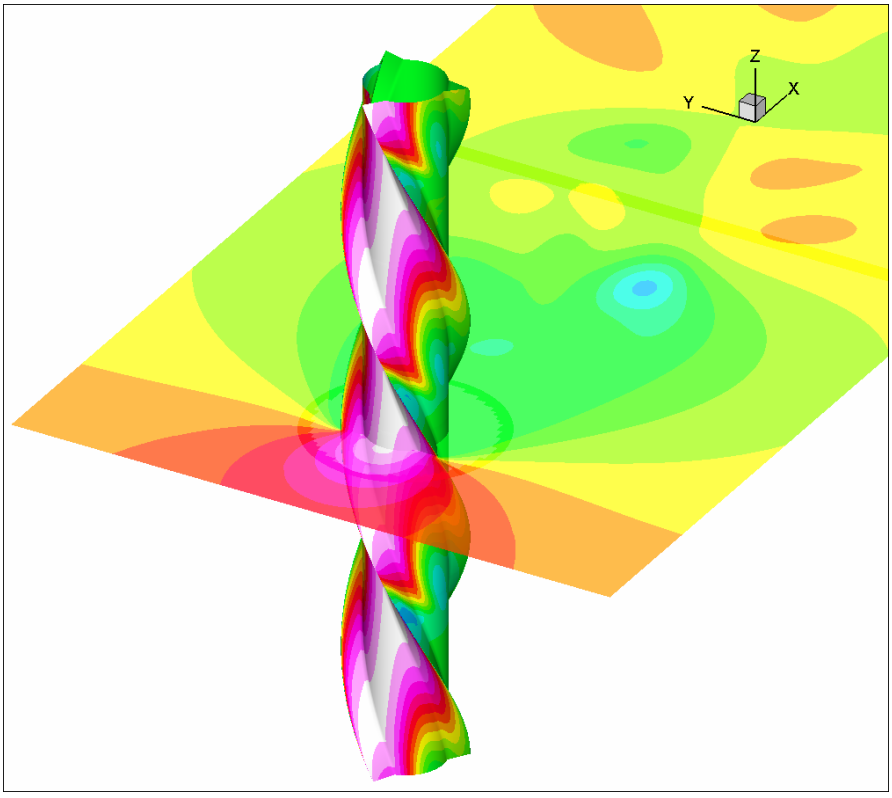


**Figure 39. Instantaneous pressure contours for flow past a fixed straked riser.**

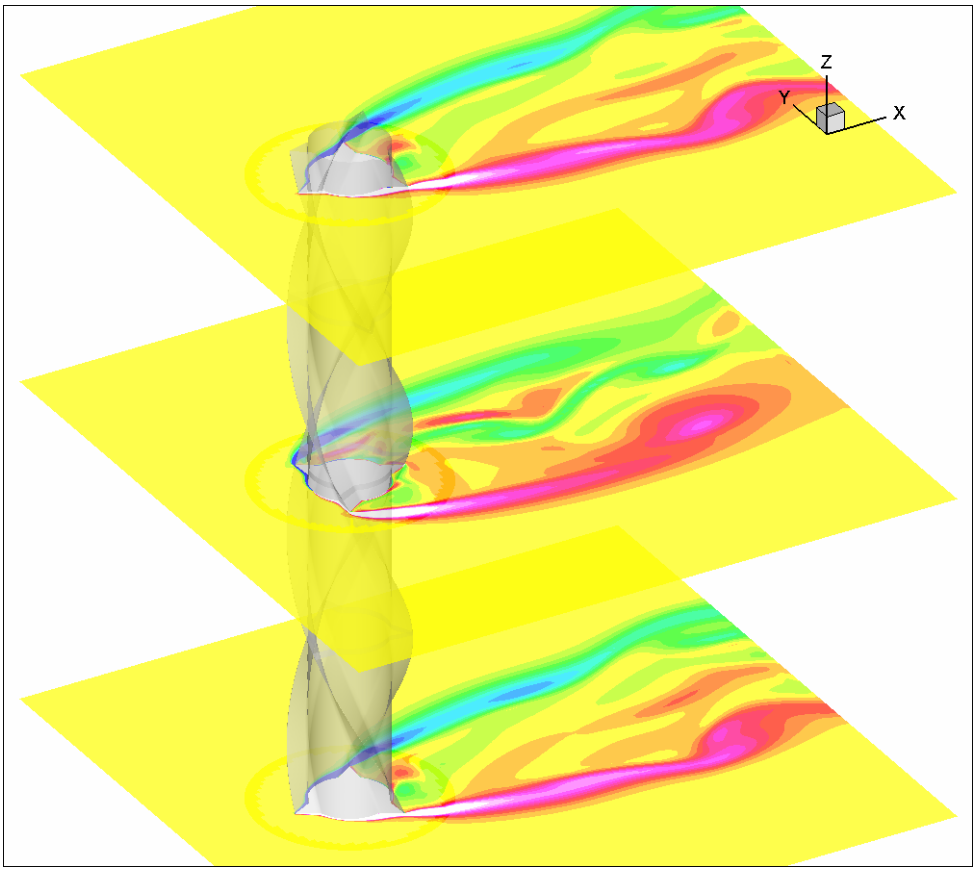


**Figure 40. Instantaneous spanwise vorticity contours, in different spanwise cross-sections, for flow past a fixed straked riser.**

In Figure 41 we show the time history of the instantaneous lift and drag coefficients for bare and straked (fixed) riser cases. In general, the helical strakes cause earlier boundary layer separation with a wider wake. This leads to an increase of average drag coefficient as shown in Figure 41. However, the helical strakes also change the phase angle of the separation line along the span and prevent the development of a coherent vortex shedding pattern with a dominant frequency. Due to partial cancellation of the out-of-phase lift forces at different spanwise positions, the lift coefficient for the straked riser is much smaller than that for the bare riser. It is clearly seen from Figure 41 that the helical strakes are very effective in suppressing any dominant shedding frequency.

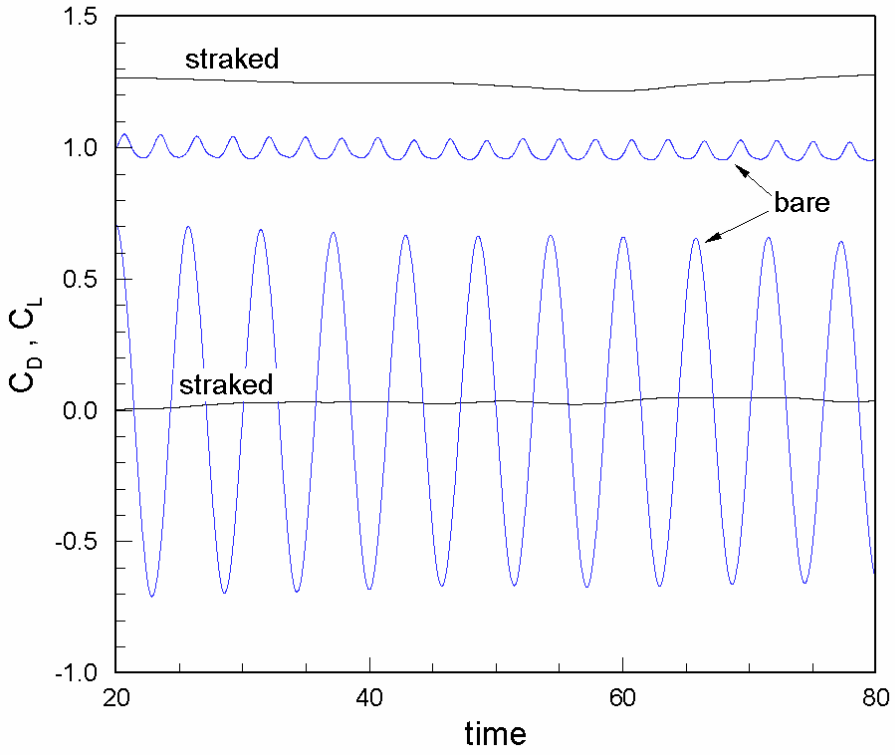


**Figure 41. Time history of instantaneous lift and drag coefficients for (fixed) bare and straked cases.**

We now consider the response of an elastically mounted straked riser, for low mass ratio and low damping. The values for the mass ratio, damping ratio, and reduced velocity used for the simulations in this study are: $m^*$=1.0, $\zeta^*$= 0.005 and $U^*$ = 6.055.

Figure 42 shows the X-Y response of the straked riser, where we also plot the response of the bare riser for comparison. We see that the helical strakes are effective in suppressing VIV. In Figure 43 we show the time history of the instantaneous lift and drag coefficients for elastically mounted bare and straked riser cases. We see that the helical strakes are once more effective in suppressing any dominant shedding frequency, and that the average drag coefficient for the straked riser is smaller than that for the bare riser.

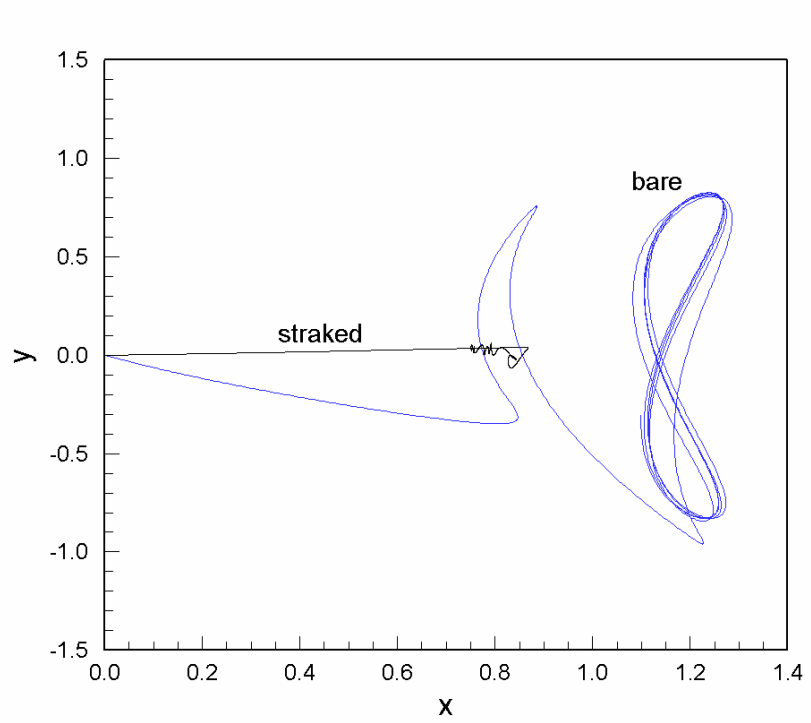


**Figure 42. X-Y response of elastically mounted bare and straked risers.**

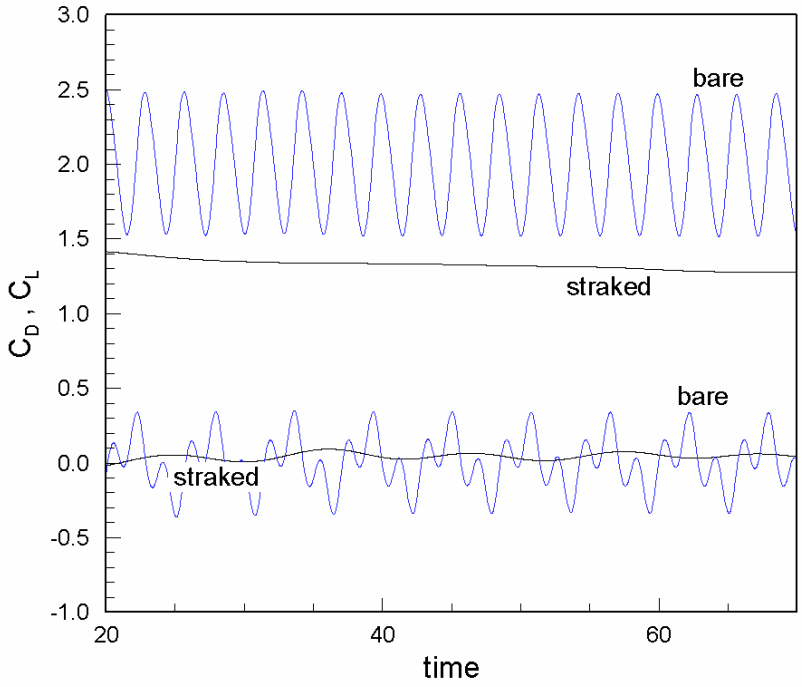


**Figure 43. Time history of instantaneous lift and drag coefficients for elastically mounted bare and straked cases.**

# Summary and Conclusions

The objective of this research was to demonstrate the use of advanced CFD capabilities for the prediction of riser VIV responses at high Reynolds number and its suppression using helical strakes and fairings. The numerical results were encouraging and display the physical behavior that has been observed in experimental set-ups and offshore; namely the stable "figure-of-eight" patterns for bare risers and VIV suppression by using fairings or helical strakes.

Having established and demonstrated the capabilities of the computational methodology, a necessary next step is to numerically map the amplitude response versus the reduced velocity for a range of reduced velocities and Reynolds numbers, to compare with available experimental data. This would further validate the present numerical methodology and establish a higher level of confidence in the CFD results presented here. In addition, it remains to be established if simulations of 2D or 3D (short-aspect ratio) risers are representative of the flow physics encountered in practical applications.

Relevant findings and important milestones of the present study are listed below, pointing to sections within the report for additional details:

1. First numerical simulation of an elastically mounted riser showing the 2T mode of vortex shedding (Section 5.1).
2. First numerical simulations of multi-riser VIV in different arrangements of up to four risers (Section 5.2 – 5.5).
3. For bare and fairing-outfitted 2D risers at Re ~ $10^5$, LES and DNS (without sub-grid scale model) predicted the same VIV responses since the near-wall grid is fine enough to resolve the smallest turbulence scales (Section 5, Section 8).
4. LES or RANS are needed for high Reynolds number (Re ~ $10^6$) cases to resolve the small scale turbulence in the wall region (Section 5, Section 8).
5. LES or RANS are needed for 3D simulations in transitional (Re ~ $10^5$) and fully turbulent regions since the grid in the spanwise direction is too coarse to resolve the smallest turbulence scales (Sections 6, 7 and 9).
6. LES improves the prediction of drag coefficient for fixed 3D riser by 10% at Re = $10^5$ in comparison with DNS (Section 6).
7. The three-dimensional effects for a riser undergoing VIV are extremely important due to the coherent turbulence structures along the span (Section 7 and Table 1).
8. Successful simulations of VIV suppression using fairings (Section 8).
9. Performance of fairings is very sensitive to torsional stiffness (Section 8).
10. Full 3D simulations of VIV suppression using helical strakes (Section 9).

In addition to the above findings, there are several important issues that warrant further investigation:

1. More computer resource are needed to facilitate the numerical simulations for realistic L/D ratios (L/D ~ 1,000 – 10,000). Access to more parallel processors and optimization of numerical grids are needed to achieve large L/D for 3D simulations.
2. There is a need to develop more advanced roughness models for massively separated flows that avoid the parameterization based on the wall shear-stress which is not defined at separation (Section 4).
3. VIV displacement response, as calculated using a full 3D model, is very sinusoidal despite the fact that the fluid-induced forcing is non-sinusoidal (Section 7). A detailed analysis of 3D velocity, pressure, and vorticity fields is needed to provide a better understanding of the fluid-structure interaction for 3D risers.

## Acknowledgements

The authors wish to thank the financial support provided by the Offshore Technology Research Center through its Cooperative Research Agreement with the Minerals Management Service. Computations were performed using resources from the Texas A&M University supercomputing facilities. Their support is gratefully acknowledged.

# References


Achenbach, E. (1968), "Distribution of Local Pressure and Skin Friction around a Circular Riser in Crossflow up to Re=$5\times10^6$," *J. Fluid Mechanics*, Vol. 34, pp. 625-639.

Al-Jamal, A. and Dalton, C. (2004), "Vortex Induced Vibrations Using Large Eddy Simulation at a Moderate Reynolds Number," *Journal of Fluids and Structures*, Vol. 19, pp. 73-92.

Bearman, P.W. (1969), "On Vortex Shedding from a Circular Riser in the Critical Reynolds Number Regime," *J. Fluid Mechanics*, Vol. 37, pp. 577-585.

Blackburn, H.M., Govardhan, R.N. and Williamson, C.H.K. (2000), "A Complimentary Numerical and Physical Investigation of Vortex-Induced Vibration," *J. Fluids and Structures*, Vol. 15, pp. 481-488.

Breuer, M (2000), "A Challenging Test for Large Eddy Simulation: High Reynolds Number Circular Riser Flow," *Int. J. Heat and Fluid Flow*, Vol. 21, pp 648-654.

Catalano, P., Wang, M., Iaccarino, G. and Moin, P. (2003), "Numerical Simulations of Flow around a Circular Riser at High Reynolds Numbers," *Int. J. Heat and Fluid Flow*, Vol. 24, pp. 463-469.

Chen, H.C. and Patel, V.C. (1988), "Near-Wall Turbulence Models for Complex Flows Including Separation." *AIAA Journal,* Vol. 26, No. 4, pp. 641-648.

Chen, H.C., Patel, V.C. and Ju, S. (1990), "Solutions of Reynolds-Averaged Navier-Stokes Equations for Three-Dimensional Incompressible Flows," *Journal of Computational Physics*, Vol. 88, No. 2, pp. 305-336.

Dong, S. and Karniadakis, G.E. (2005), "DNS of Flow Past a Stationary and Oscillating Riser at Re=10 000," *J. Fluids and Structures*, Vol. 20, pp. 519-531.

Durbin, P.A., Medic, G., Seo, J.M., Eaton, J.K. and Song, S. (2001), "Rough Wall Modification of Two-Layer k-ε," *Journal of Fluid Engineering*, Vol. 123, pp. 16-21.

Farrant, T., Tan, M. and Price, W.G. (2000), "A Cell Boundary Element Method Applied to Laminar Vortex Shedding from Arrays of Risers in Various Arrangements," *Journal of Fluids and Structures*, Vol. 14, pp. 375-402.

Guilmineau, E. and Queutey, P. (2004), "Numerical Simulation of Vortex-Induced Vibration of a Circular Riser with Low Mass-Damping in a Turbulent Flow," *Journal of Fluids and Structures*, Vol. 19, pp. 449-466.

Holmes, S., Constantinides, Y. and Oakley, O.H. (2006), "Simulation of Riser VIV using Fully Three Dimensional CFD Simulations," OMAE2006-92124, Proceedings, 25th International Conference on Offshore Mechanics and Arctic Engineering, June 4-9, 2006, Hamburg, Germany.

Jauvtis, N and Williamson, C.H.K. (2004), "The Effects of Two Degrees of Freedom on Vortex-Induced Vibrations at Low Mass and Damping," *J. Fluid Mechanics*, Vol. 509, pp. 23-62.

Jeon, D. and Gharib, M. (2001), "On Circular Risers Undergoing Two-Degree-of-Freedom forced Motions," *J. of Fluids and Structures*, Vol. 15, pp. 533-541.

Mittal, S. and Kumar, V. (2004), "Vortex Induced Vibrations of a Pair of Circular Risers at Reynolds Number 1000," *International Journal of Computational Fluid Dynamics*, Vol. 18, pp. 601-614.

Norberg, C. (2001), "Flow around a Circular Riser: Aspects of Fluctuating Lift," *J. Fluids and Structures*, Vol. 15, pp. 459-469.

Patel, V.C. and Yoon, J.Y. (1995), "Application of Turbulence Models to Separated Flow Over Rough Surfaces," *Journal of Fluids Engineering*, Vol. 117, No. 2, pp. 234-241.

Pontaza, J.P., Chen, H.C. and Reddy, J.N. (2005), "A Local-Analytic-Based Discretization Procedure for the Numerical Solution of Incompressible Flows." *Int. Journal for Numerical Methods in Fluids*, Vol. 49, pp. 657-699.

Schewe, G. (1983), "On the Force Fluctuations Acting on a Circular Riser in Crossflow from Subcritical up to Transcritical Reynolds Number," *J. Fluid Mechanics*, Vol. 133, pp. 265-285.

Williamson, C.H.K (1985), "Evolution of a Single Wake behind a Pair of Bluff Bodies," *Journal of Fluid Mechanics*, Vol. 159, pp 1-18.

Williamson, C.H.K. and Jauvtis, N. (2004), "A High-Amplitude 2T Mode of Vortex-Induced Vibration for a Light Body in XY Motion," *European Journal of Mechanics B/Fluids*, Vol. 23, pp. 107-114.

Zdravkovich, M.M. (2003), *Flow around circular risers*, Vol. 2, Oxford University Press.

## Publications Under Project

*Conference papers:*


1. Pontaza J.P., Chen, C.R. and Chen H.C. (2004), "Chimera Reynolds-Averaged Navier-Stokes Simulation of Vortex-Induced Vibrations of Circular Risers," Proceedings of *Civil Engineering in the Oceans VI Conference*, October 20-22, Baltimore, Maryland.

2. Pontaza J.P., Chen, C.R. and Chen H.C. (2005), "Simulations of High Reynolds Number Flow past Arrays of Risers Undergoing Vortex-Induced Vibrations," 15th International Offshore and Polar Engineering Conference, Vol. II, pp. 201-207, 19-24 June, Seoul, Korea.

3. Pontaza J.P., Chen, H.C. and Chen, C.R. (2005), "Numerical Simulations of Riser Vortex-Induced Vibrations." Proceedings of Society of Naval Architecture and Marine Engineering (SNAME) Conference, Paper #D52-2005, October, Houston, Texas

4. Pontaza J.P. and Chen, H.C. (2006), "Numerical Simulations of Circular Risers Outfitted with Vortex-Induced Vibrations Suppressors," 16th International Offshore and Polar Engineering Conference, May 28-June 2, San Francisco, California.

5. Pontaza J.P. and Chen, H.C. (2006), "Three-dimensional Numerical Simulations of Circular Risers Undergoing Two Degree-of-Freedom Vortex-Induced Vibrations," OMAE 2006-92052, Proceedings of 25th International Conference on Offshore Mechanics and Artic Engineering, June 4-9 , Hamburg, Germany.


*Journal papers:*


6. Pontaza, J.P., Chen, H.C. and Reddy, J.N. (2005), "A Local-Analytic-Based Discretization Procedure for the Numerical Solution of Incompressible Flows," *International Journal for Numerical Methods in Fluids*, Vol. 49, pp. 657-699.

7. Pontaza, J.P. and Chen, H.C., "Three-Dimensional Numerical Simulations of Circular Risers Undergoing Two Degree-of-Freedom Vortex-Induced Vibrations," *ASME Journal of Offshore Mechanics and Arctic Engineering*, accepted.